Nikkhoo, M., Walter, T. R. (2015): Triangular dislocation: an analytical, artefact-free solution. - *Geophysical Journal International*, *201*, 2, p. 1119-1141.

DOI: http://doi.org/10.1093/gji/ggv035

Geophysical Journal International

Geophys. J. Int. (2015) **201,** 1119–1141 doi: 10.1093/gji/ggv035
GJI Geodynamics and tectonics

Triangular dislocation: an analytical, artefact-free solution

Mehdi Nikkhoo and Thomas R. Walter

Department of Physics of the Earth, Helmholtz-Centre Potsdam, GFZ German Research Centre for Geosciences, Telegrafenberg, D-14473 Potsdam, Germany. E-mail: mehdi.nikkhoo@gfz-potsdam.de

Accepted 2015 January 16. Received 2015 January 14; in original form 2014 October 26

SUMMARY

Displacements and stress-field changes associated with earthquakes, volcanoes, landslides and human activity are often simulated using numerical models in an attempt to understand the underlying processes and their governing physics. The application of elastic dislocation theory to these problems, however, may be biased because of numerical instabilities in the calculations. Here, we present a new method that is free of artefact singularities and numerical instabilities in analytical solutions for triangular dislocations (TDs) in both full-space and half-space. We apply the method to both the displacement and the stress fields. The entire 3-D Euclidean space $\mathbb{R}^3$ is divided into two complementary subspaces, in the sense that in each one, a particular analytical formulation fulfils the requirements for the ideal, artefact-free solution for a TD. The primary advantage of the presented method is that the development of our solutions involves neither numerical approximations nor series expansion methods. As a result, the final outputs are independent of the scale of the input parameters, including the size and position of the dislocation as well as its corresponding slip vector components. Our solutions are therefore well suited for application at various scales in geoscience, physics and engineering. We validate the solutions through comparison to other well-known analytical methods and provide the MATLAB codes.

Key words: Geomechanics; Kinematics of crustal and mantle deformation.

1 INTRODUCTION

Crustal deformations associated with earthquakes, volcanoes, landslides and human activities can be observed at a high level of detail using modern geodetic techniques, including synthetic aperture radar interferometry (InSAR) and GPS (Segall 1997; Bürgmann *et al.* 2000). These deformation data are often analysed using modelling techniques that are typically very computationally intense. The primary objective of such modelling is to understand the underlying processes through indirect imaging of the so-called sources, such as seismogenic faults, magma chambers and other reservoirs. The position and geometry of these sources, as well as the slip or the forces acting on them, are typically regarded as the source parameters. The source parameters, in other words, the outputs of the implemented modelling, are relevant to earthquake aftershock studies, the assessment of volcanic eruption precursors, tsunami modelling and many other applications (Feigl *et al.* 2002).

The majority of methods that are applied for crustal deformation modelling are based on the theory of elasticity in general and the concept of dislocations in particular (Segall 2010). Elastic dislocation theory concerns the state of deformations in a strained solid body that is subject to the action of a dislocation embedded inside it (Love 1944). The Volterra model (Volterra 1907) describes a dislocation as a surface of displacement discontinuity with a uniform distribution of the slip throughout. The edges of the Volterra dislocation, also known as dislocation lines, are intrinsic singularities because of their corresponding displacements, which are essentially indeterminate (Steketee 1958). Consequently, the displacements, strains and stresses are singular on the dislocation lines, and numerical calculations are instable in the vicinity of these singularities.

Apart from these singular dislocation lines and their differential neighbourhoods, the analytical solutions of the general Volterra dislocations are continuous and well-behaved functions elsewhere, including the dislocation surface itself (Segall 2010). In geophysics, Volterra's dislocation theory is therefore used extensively, following the Green's function method of Steketee (1958), which describes a general point-source dislocation in an isotropic elastic half-space.

Integration of the fundamental point-source dislocations gives rise to analytical solutions for finite dislocations such as rectangular dislocations (RDs; Okada 1992) or triangular dislocations (TDs; Jeyakumaran *et al.* 1992; Meade 2007). Since the derivation of these solutions, they have been used directly as simple analytical models and also as the basis for more sophisticated numerical models, such as

distributed slip models (Wald & Heaton 1994) and the boundary element method (BEM; Cayol & Cornet 1997). The possibility of simulating any arbitrarily curved surface in terms of a continuous triangular mesh is a clear advantage of the implementation of the TD approach over the RD approach and has led to the consideration of complex dislocation geometries (Maerten *et al.* 2005; Meade 2007).

However, the existence of the artefact singularities and numerical instabilities that affect the calculation of the displacements and stresses associated with a TD has posed an obstacle to the geometrical flexibility and applicability of TDs. The more TDs are present in a model, the higher is the probability of obtaining erroneous results at various calculation points. Therefore, an artefact-free solution for TDs is of great relevance. In contrast to the intrinsic singularities, there is no theoretical basis to explain the artefact singularities, which are produced only through imperfections in numerical calculation. The analytical solutions for TDs are derived either through direct analytical integration over the surface of the triangle (Crouch & Starfield 1983) or by superposing basic dislocations with known analytical solutions, as has been considered for segment dislocation in a full-space (Hirth & Lothe 1982), angular dislocation in a full-space (Yoffe 1960) and angular dislocation in a half-space (Comninou & Dundurs 1975). A general problem that is encountered in either case, however, is related to the artefact singularities and numerical instabilities that lie along the sides of a TD in a full-space and also below and above the vertices of a TD in a half-space. Despite a few previous attempts, in which either the artefact singularities have been addressed only in part (Thomas 1993) or a combination of analytical and numerical quadrature rules along with a Taylor series expansion has been proposed to approximately correct for the effects of the artefact singularities (Gimbutas *et al.* 2012), the problem of artefact singularities for TDs has not yet been analytically addressed. Cai *et al.* (2006) have summarized some methods that attempt to address the intrinsic singularities and have also developed a novel, elegant formulation for the stress field of a segment dislocation in a full-space. Although this solution is free of intrinsic and artefact singularities, it lacks the displacement equations and is not applicable to a half-space (Cai *et al.* 2006).

In this paper, we present a fully analytical, artefact-free solution for the displacement and the strain and stress fields associated with a TD in a full-space and half-space. This paper is organized as follows:

First, we generalise the solution, following (Yoffe 1960), to a generic TD in a full-space and elaborate on the necessary coordinate systems and transformations. Secondly, we address the problem of artefact singularities and numerical instabilities along with presenting the analytical solution for a TD in a full-space (Yoffe 1960). We then use the full-space artefact-free solution to develop an analytical artefact-free solution for a TD in a half-space. Finally, we evaluate our solution through comparison to other analytical solutions for finite dislocations, followed by a discussion section.

2 A TRIANGULAR DISLOCATION IN A FULL-SPACE

The full-space solution is a relatively simple model that not only can be directly used in several geophysical applications but also is the basis for the more realistic half-space model (Comninou & Dundurs 1975). Additionally, as the basis for numerical approaches such as the BEM, the full-space solution can be used to simulate realistic topography in related models (Cayol & Cornet 1997). Here, we develop a generic solution for a triangular dislocation (TD) in a full-space as a superposition of three angular dislocations, following Yoffe (1960), and elaborate on the necessary coordinate systems and the coordinate transformations between them. The implemented coordinate transformation scheme, which is the most fundamental concept underlying the development of the solution, is detailed in Appendix A. We also develop a so-called 'alternative solution' that is equivalent to the first solution but possesses singularities along completely different directions. Using a geometric technique, we present an artefact-free solution that is a combination of these two equivalent solutions. Improvements on the Burgers function equation are used in the displacement calculations associated with a TD. These new improvements allow for faster calculations and eliminate the numerical instabilities in the calculation of the Burgers function in the Yoffe (1960) solution.

2.1 The general solution for a TD in a full-space

2.1.1 The structure of the solution

An angular dislocation is composed of two semi-infinite straight dislocation lines that meet at the point of origin (Fig. 1a). The analytical solution of an angular dislocation in a full-space was first developed by Yoffe (1960), employing Burgers' method (Burgers 1939). The equations of the displacement and stress field of an angular dislocation, which we have corrected for a few misprints, are provided in Appendix B accompanying this paper. These equations are valid in the angular dislocation coordinate system (ADCS), which is a right-handed Cartesian coordinate system with the x-axis normal to the page (Fig. 1a). Here, the coordinates of the Burgers vector of the angular dislocation represented by (b_x, b_y, b_z) are composed of the opening and slip components along the y and z directions, respectively. The Burgers vector, also known as the slip vector, essentially represents the relative motion of the two sides of a dislocation.

Yoffe (1960) also derived the first analytical solution for a particular case of an equilateral TD in a full-space by superposing the displacement and stress fields of the three angular dislocations that form the exterior angles of the TD (Fig. 1b). All three angular dislocations share the same slip vector, which is the slip vector of the TD. Here, we generalize the solution, following Yoffe (1960), to a generic TD in a full-space and elaborate on the details of our work.

We specify the components of the slip vector of the TD, that is the strike slip, the dip slip and the opening, with respect to the triangular dislocation coordinate system (TDCS). The TDCS is a right-handed Cartesian coordinate system with the second vertex of the TD as its origin (Fig. 1b). The y-, z- and x-axes of the TDCS align with the strike, dip and normal to the TD directions. We consider the same conventions for

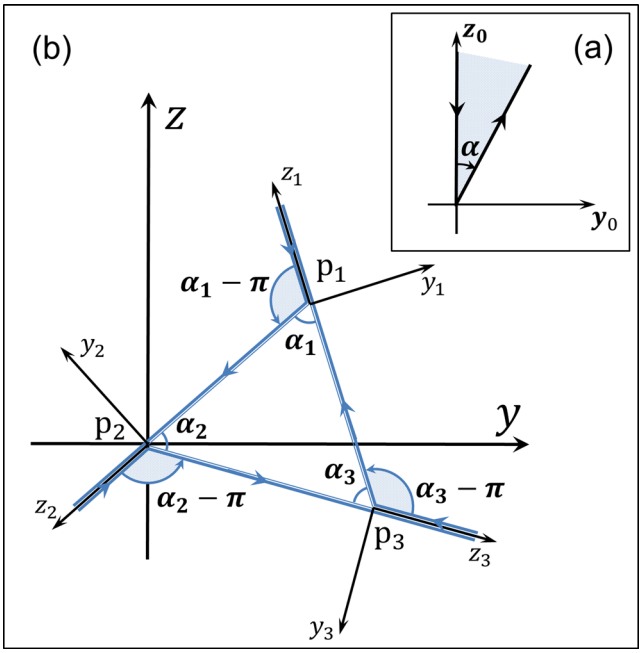

Figure 1. (a) Angular dislocation in a full-space following Yoffe (1960); the x_0-axis is perpendicular to the plane and forms a right-handed coordinate system. The angle α is measured clockwise. (b) Yoffe (1960) configuration for a triangular dislocation (TD) in a full-space. It consists of the three angular dislocations that form the external angles of the triangle $P_1P_2P_3$. The third axis of each angular dislocation coordinate system (ADCS) lies along one side of the TD, and the first axis of each of these right-handed coordinate systems is perpendicular to the plane. The x, y and z axes of the triangular dislocation coordinate system (TDCS) are normal to the plane, parallel to the strike direction and parallel to the dip vector, respectively. The vertex P_2 of the TD is the origin of the TDCS.

the strike, dip and normal directions that are defined for an RD (Okada 1985) to facilitate comparison with the RD case. For the vertices of the TD, however, as well as the calculation points, the coordinates are given in an Earth-fixed coordinate system (EFCS) with the X- and Y-axes pointing towards the east and north, respectively, and the Z-axis pointing upwards. The diagram presented in Fig. 2 summarizes all necessary coordinate transformations used in this paper. Here, we first transform the coordinates of the calculation points and the TD vertices from the EFCS into the TDCS. The next step is to transform the coordinates of the calculation points and the components of the TD slip vector from the TDCS into each ADCS separately. Then, it is possible to calculate the displacement and stress fields of each angular dislocation in its own ADCS, which, in the next step, are all transformed back into the TDCS. As the final step, after superposing the contributions of all three angular dislocations, we transform the displacement and stress field of the TD into the EFCS.

2.1.2 The implementation procedure

We adopt $\{\vec{e}_X, \vec{e}_Y, \vec{e}_Z\}$ as the basis for the EFCS, $\{\vec{e}_n, \vec{e}_s, \vec{e}_d\}$ as the basis for the TDCS, and, finally, $\{\vec{e}_{x_1}, \vec{e}_{y_1}, \vec{e}_{z_1}\}$, $\{\vec{e}_{x_2}, \vec{e}_{y_2}, \vec{e}_{z_2}\}$ and $\{\vec{e}_{x_3}, \vec{e}_{y_3}, \vec{e}_{z_3}\}$ as the bases for the three ADCSs. To apply the transformations illustrated in Fig. 2, we first determine the necessary transformation matrices (Appendix A). We also adopt the right-hand rule, that is when the curl of the fingers of the right hand represents the vertex ordering, then the normal vector of the TD points along the thumb. Therefore, if $\vec{r}_{P_1}$, $\vec{r}_{P_2}$ and $\vec{r}_{P_3}$ are the position vectors of the TD vertices in the EFCS, then the normal vector can be defined as $\vec{e}_n = (\vec{r}_{12} \times \vec{r}_{13})/\|\vec{r}_{12} \times \vec{r}_{13}\|$, which is the normalized cross product of the vectors $\vec{r}_{12} = \vec{r}_{P_2} - \vec{r}_{P_1}$ and $\vec{r}_{13} = \vec{r}_{P_3} - \vec{r}_{P_1}$, that is the vectors along the P_1P_2 and P_1P_3 sides, respectively. The unit strike vector is then defined as $\vec{e}_s = (\vec{e}_Z \times \vec{e}_n)/\|\vec{e}_Z \times \vec{e}_n\|$. Finally, $\vec{e}_d = \vec{e}_n \times \vec{e}_s$ represents the unit dip vector. As a result, the transformation matrix for the direct transformation from the TDCS into the EFCS will be

$$A_{TE} = \begin{pmatrix} X_n & X_s & X_d \\ Y_n & Y_s & Y_d \\ Z_n & Z_s & Z_d \end{pmatrix}. \tag{1}$$

The three columns of A_{TE} are the coordinates of the vectors $\vec{e}_n$, $\vec{e}_s$ and $\vec{e}_d$ in the EFCS. Recall that the origin of the TDCS is the second vertex of the TD, which is P_2; thus, the translation matrix for the direct position vector transformation in eq. (A4) is $r_{P_2} = (X_{P_2}\ Y_{P_2}\ Z_{P_2})^T$, which is precisely the coordinates of P_2 in the EFCS. For the inverse transformation in this case, we use eqs (A5) and (A9) for the free vectors and the position vectors, respectively. For the transformation of the strain and stress tensors, eq. (A10) is used.

To use the equations associated with each angular dislocation, we must transform the coordinates of the calculation points and the TD slip vector from the TDCS to each ADCS. Because the TDCS and the ADCS share the same x-axis, it is obvious that $\vec{e}_{x_1} = \vec{e}_n$. Moreover, from the configuration of the TD in Fig. 1(b), it is clear that $\vec{e}_{z_1}$ is aligned with the P_3P_1 side and thus that $\vec{e}_{z_1} = \vec{r}_{31}/\|\vec{r}_{31}\|$, where $\vec{r}_{31} = \vec{r}_{P_1} - \vec{r}_{P_3}$.

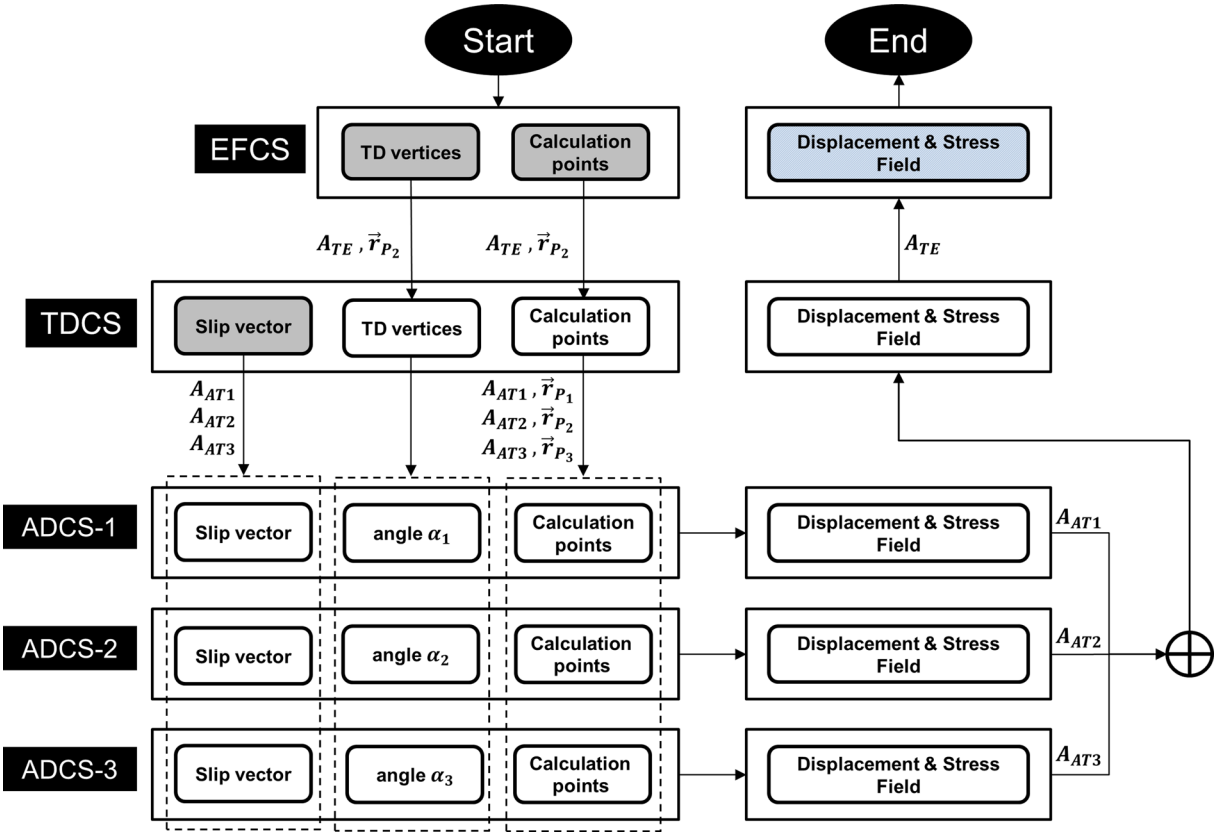

Figure 2. Flowchart for calculating the displacement and stress field of a triangular dislocation (TD) in an Earth-fixed coordinate system (EFCS) using the full-space Yoffe (1960) solution. The black box at the left side of each row specifies the coordinate system corresponding to that row. The grey boxes represent the inputs, and the blue box represents the final output. The coordinates of the calculation points and the TD vertices are first transformed from the EFCS into the triangular dislocation coordinate system (TDCS) using A_{TE} and $\vec{r}_{P_2}$ in eq. (A9). These coordinates, along with the slip vector, are then transformed into each angular dislocation coordinate system (ADCS) (see eqs A9 and A5 in Appendix A). After the contribution of each angular dislocation is calculated, the results are transformed into the TDCS (see also eqs A4 and A10 in Appendix A). Finally, the superposition of the results is transformed into the EFCS.

Because the ADCS as a right-handed coordinate system, we can write the third equation as $\vec{e}_{y_1} = \vec{e}_{z_1} \times \vec{e}_{x_1}$. The columns of the transformation matrix A_{AT_1} for the direct transformation from the first ADCS into the TDCS are the coordinates of $\vec{e}_{x_1}$, $\vec{e}_{y_1}$ and $\vec{e}_{z_1}$ in the TDCS:

$$A_{AT_1} = \begin{pmatrix} 1 & 0 & 0 \\ 0 & z_{P_1} - z_{P_3} & y_{P_1} - y_{P_3} \\ 0 & y_{P_3} - y_{P_1} & z_{P_1} - z_{P_3} \end{pmatrix}. \tag{2}$$

A_{AT_2} and A_{AT_3}, which correspond to the second and third ADCSs, are defined similarly. As the origins of the ADCSs are the vertices of the TD (Fig. 1b), the translation matrices in eq. (A4) will be the coordinates of $\vec{r}_{P_1}$, $\vec{r}_{P_2}$ and $\vec{r}_{P_3}$ in the TDCS. For the inverse transformations in these cases, we also use eqs (A5) and (A9) for the free vectors and the position vectors, respectively. For the transformation of the strain and stress tensors, we again use eq. (A10).

The size of the angle with the appropriate algebraic sign is the final input parameter that we need to calculate for each angular dislocation. The internal angles of the TD can be calculated as follows:

$$\alpha_1 = \cos^{-1}(\vec{e}_{12}.\vec{e}_{13})$$

$$\alpha_2 = \cos^{-1}(\vec{e}_{21}.\vec{e}_{23})$$

$$\alpha_3 = \cos^{-1}(\vec{e}_{13}.\vec{e}_{23}),$$

where $\vec{e}_{12} = (\vec{r}_{P_2} - \vec{r}_{P_1})/\|\vec{r}_{P_2} - \vec{r}_{P_1}\|$, $\vec{e}_{13} = (\vec{r}_{P_3} - \vec{r}_{P_1})/\|\vec{r}_{P_3} - \vec{r}_{P_1}\|$ and $\vec{e}_{23} = (\vec{r}_{P_3} - \vec{r}_{P_2})/\|\vec{r}_{P_3} - \vec{r}_{P_2}\|$ are the unit vectors along the sides of the TD and ' . ' represents the dot product of the vectors. The angles that must be used in the calculations are the supplementary angles of α_1, α_2 and α_3 measured clockwise, that is $\alpha_1 - \pi$, $\alpha_2 - \pi$ and $\alpha_3 - \pi$, respectively (Fig. 1b).

Now, we calculate the 'incomplete' displacements (see Appendix B) and the stresses associated with each angular dislocation using eqs (B2) and (B4), respectively. Subsequently, after transforming the results from each ADCS into the TDCS, we calculate the complete

displacements as follows:

$$u = b_x \varphi_{TD} + \sum_{i=1}^{3} u_i^0$$

$$v = b_y \varphi_{TD} + \sum_{i=1}^{3} v_i^0$$

$$w = b_z \varphi_{TD} + \sum_{i=1}^{3} w_i^0, \tag{3}$$

where u_i^0, v_i^0 and w_i^0 are the components of the incomplete displacements of the ith angular dislocation and φ_{TD} is the Burgers function (Burgers 1939) that corresponds to the TD. We elaborate on the calculation of φ_{TD} in Section 2.3. Note that in eq. (3), we use the components of the slip vector and the incomplete displacement vector in the TDCS. The outcome of this step is the displacement and stress fields of the TD in the TDCS. As a final step, we transform these results into the EFCS.

2.2 Developing an artefact-free solution for a TD in a full-space

The analytical solutions for a TD in a full-space contain artefact singularities on the extensions of the sides of the TD (Kuriyama & Mizuta 1993). Similar difficulties also exist in the general solution of the previous section. In the following, we describe a geometric method for developing a fully analytical solution that is free of such artefact singularities.

The semi-infinite dislocation lines with opposite polarities that are shown in Fig. 1(b) must theoretically cancel each other outside the TD. However, because the contribution of each angular dislocation is calculated separately, the singular terms in the displacement and stress equations remain in the final results, giving rise to artefact singularities. Moreover, each dislocation line possesses a $1/r$ singularity, where r is the distance from the dislocation line (Segall 2010). Therefore, numerical instabilities are also observed everywhere in the vicinity of the semi-infinite dislocation lines.

As the first step in eliminating the artefact singularities, we reconfigure the angular dislocations as illustrated in Fig. 3. The input parameters of both configurations are presented in Table 1. Clearly, these two solutions are equivalent. The artefact singularities in these two configurations, however, occur in completely different locations. As a result, if the calculation point, for example, point P in Fig. 3(a), lies on or in the vicinity of the lines of the artefact singularities, we can successfully avoid any computational problems by using the other configuration depicted in Fig. 3(b).

To choose between the two configurations for any arbitrary calculation point, we consider the orthogonal projection of the point onto the TD plane, which we hereafter refer to as 'the projection point'. We also subdivide the plane of the TD into six partitions using the medians of the TD sides (Fig. 4). When this approach is taken, each line of artefact singularity is located in one and only one of the six partitions. For the projection points outside the TD, we use the configuration whose lines of artefact singularity do not lie in the same partition as the projection point. For the projection points inside the TD, either configuration can be used. Following this strategy, we always maintain the maximum distance from the dislocation lines, regardless of whether the point of calculation lies on the plane of the TD. As a consequence, we avoid both artefact singularities and numerical instabilities for any on- or off-plane calculation points.

To implement this strategy, we must be able to identify the partition in which the projection point is located. For this purpose, we use the special barycentric coordinates of the projection points (Ungar 2010). The barycentric coordinate system efficiently represents the coordinates of points in the plane of a triangle with respect to the position of the vertices of the triangle. Further details concerning the barycentric coordinate system can be found in Appendix C. The very simple and often symmetric form of the equations of geometric shapes in this coordinate system makes it the most appropriate system for many problems related to the geometrical properties of a triangle (Bottema 2008).

For an arbitrary point $P(x_P, y_P)$ and a triangle with vertices $A_1(x_1, y_1)$, $A_2(x_2, y_2)$ and $A_3(x_3, y_3)$ in a 2-D Cartesian coordinate system, the normalized barycentric coordinates (μ_1, μ_2, μ_3) of P with respect to $A_1A_2A_3$ are calculated as follows:

$$\mu_1 = \frac{\begin{vmatrix} x_P - x_3 & x_2 - x_3 \\ y_P - y_3 & y_2 - y_3 \end{vmatrix}}{\begin{vmatrix} x_1 - x_3 & x_2 - x_3 \\ y_1 - y_3 & y_2 - y_3 \end{vmatrix}}, \tag{4}$$

$$\mu_2 = \frac{\begin{vmatrix} x_1 - x_3 & x_P - x_3 \\ y_1 - y_3 & y_P - y_3 \end{vmatrix}}{\begin{vmatrix} x_1 - x_3 & x_2 - x_3 \\ y_1 - y_3 & y_2 - y_3 \end{vmatrix}}, \tag{5}$$

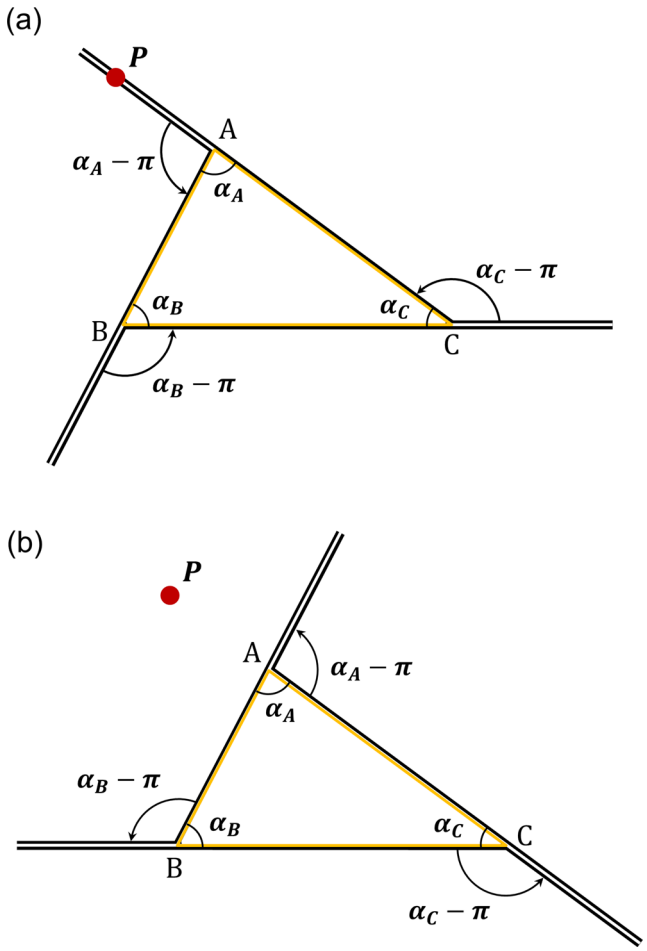

Figure 3. Two different configurations for the triangular dislocation *ABC*. Apart from the placements of the semi-infinite dislocation lines, these configurations are equivalent and can be used interchangeably. (a) The calculation point *P* in the plane of the triangle intersects one of the dislocation lines. (b) In the 'alternative' configuration for the angular dislocations, point *P* is located at the maximum possible distance from such lines. Through the selection of the appropriate configuration, any artefact singularity or numerical instability can be avoided.

Table 1. The parameters of the two configurations illustrated in Fig. 3.

	Angular dislocation vertex	Input angle	*z*-axis direction
Config-1	P_1	$-\pi + \alpha_1$	P_3P_1
	P_2	$-\pi + \alpha_2$	P_1P_2
	P_3	$-\pi + \alpha_3$	P_2P_3
Config-2	P_1	$-\pi + \alpha_1$	P_1P_3
	P_2	$-\pi + \alpha_2$	P_2P_1
	P_3	$-\pi + \alpha_3$	P_3P_2

and

$$\mu_3 = 1 - \mu_1 - \mu_2, \tag{6}$$

where the symbol '|.|' represents the determinant of the matrix. The equations $\mu_1 = \mu_2$, $\mu_1 = \mu_3$ and $\mu_2 = \mu_3$ represent the medians of the triangle (Ungar 2010). Using this equations and the barycentric coordinates of each projection point with respect to the TD vertices, we developed a set of simple inequalities that enable us to identify the partition corresponding to each projection point. The inequalities corresponding to the partitions illustrated in Fig. 4 are summarized in Table 2. The necessary computation time for the transformation of the primary Cartesian coordinates into the barycentric coordinate system is negligible.

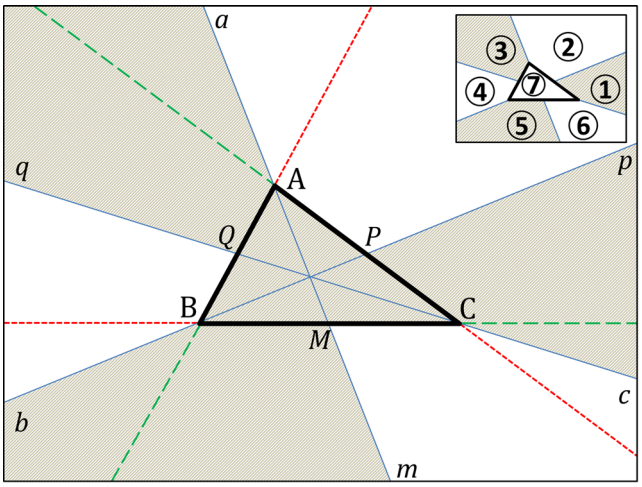

Figure 4. The seven partitions in the plane of the triangular dislocation (TD) formed by *AM*, *BP* and *CQ*, which are the medians of the TD extended through the plane on both sides (the solid concurrent lines). The green dashed lines and the red dotted lines represent the lines of singularities corresponding to the two configurations of Fig. 3. Each line of singularity lies in only one of the partitions. To avoid artefact singularities and numerical instabilities, we use the configuration corresponding to the red dotted lines for the projection points that lie in the dark partitions and the configuration corresponding to the green dashed lines for the remaining points. Either configuration can be used for the points inside the TD. The subpanel on the top right shows the numbers assigned to the partitions, which are used in Table 2.

Table 2. The inequalities that define the partitions in the special barycentric coordinate system illustrated in Fig. 4.

Zone number	Zone corners	Inequalities specifying the zone I	II	III	Artefact-free configuration in the zone
1	*cCPp*	$\mu_3 \geq \mu_1$	$\mu_1 \geq \mu_2$	$\mu_2 < 0$	Config-2
2	*pPAa*	$\mu_1 \geq \mu_3$	$\mu_3 \geq \mu_2$	$\mu_2 < 0$	Config-1
3	*aAQq*	$\mu_1 \geq \mu_2$	$\mu_2 \geq \mu_3$	$\mu_3 < 0$	Config-2
4	*qQBb*	$\mu_2 \geq \mu_1$	$\mu_1 \geq \mu_3$	$\mu_3 < 0$	Config-1
5	*bBMm*	$\mu_2 \geq \mu_3$	$\mu_3 \geq \mu_1$	$\mu_1 < 0$	Config-2
6	*mMCc*	$\mu_3 \geq \mu_2$	$\mu_2 \geq \mu_1$	$\mu_1 < 0$	Config-1
7	*ABC*	$\mu_1 > 0$	$\mu_2 > 0$	$\mu_3 > 0$	Config-1 and Config-2

2.3 Improvement on the Burgers function formulation

The Burgers function (Burgers 1939), which appears in the displacement equations associated with any dislocation, is the only term that allows for a discontinuity across the dislocation surface (Brown 1975). The strain and stress equations, however, as functions of the partial derivatives of the displacements, include the partial derivatives of the Burgers function.

For an arbitrary calculation point $P(x_P, y_P, z_P)$, the Burgers function φ^P is proportional to the solid angle Ω^P subtended at P by the dislocation (Burgers 1939):

$$\varphi^P = \frac{\Omega^P}{4\pi}. \tag{7}$$

In other words, the dislocation is observed from the point P through the solid angle.

To calculate the displacements associated with a TD, we use eq. (3). Yoffe (1960) calculated the Burgers function corresponding to a TD, that is φ^P_{TD}, in terms of the superposition of the Burgers functions of three angular dislocations forming a configuration such as that illustrated in Fig. 1(b). This approach, however, results in an incorrect value for $\varphi^P_{\rm TD}$ because the angular dislocations are the external angles of the TD, and therefore, the calculated $\varphi^P_{\rm TD}$ corresponds to the entire $x = 0$ plane except the TD surface.

In the following, we apply the equation developed by Van Oosterom & Strackee (1983) to calculate $\varphi^P_{\rm TD}$, which is the Burgers function associated with the TD. Using the same equation, we then develop a new equation for φ^P_A, which is the Burgers function associated with the angular dislocation. Eventually, we verify our approach by calculating and comparing the partial derivatives of our new equation for φ^P_A to the Yoffe (1960) equations.

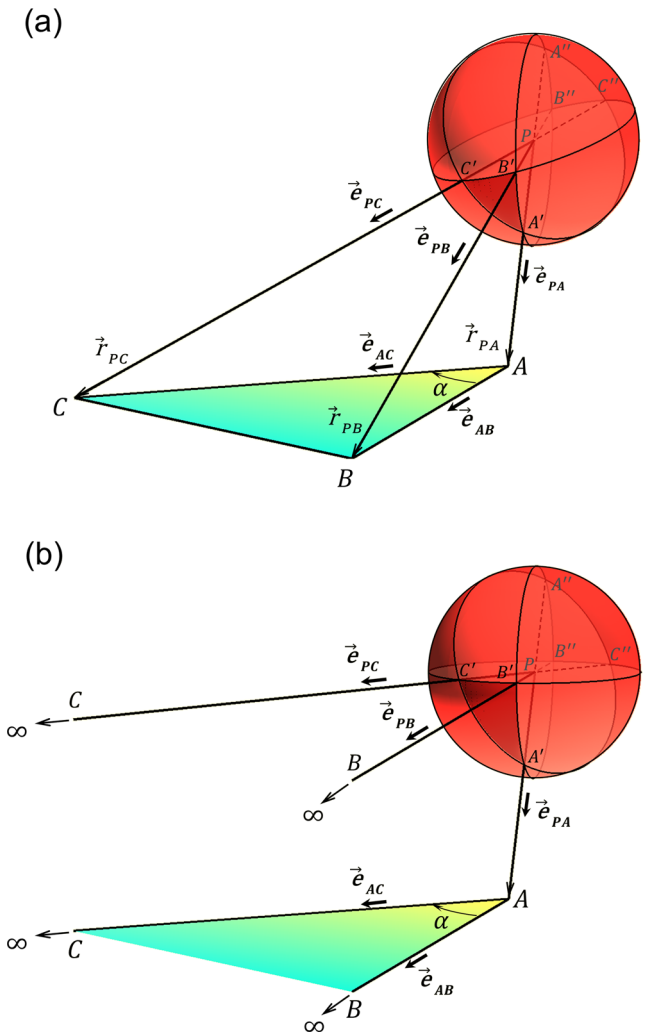

Figure 5. (a) The solid angle subtended at point P, the centre of the unit sphere, by the triangular dislocation ABC. This solid angle is equal to the area of the spherical triangle $A'B'C'$, which is the orthogonal projection of the TD onto the unit sphere. (b) The solid angle subtended at point P by the angular dislocation A, shown as the limit of the TD solid angle as the vertices B and C approach infinity along the positive directions of $\vec{e}_{AB}$ and $\vec{e}_{AC}$, respectively. By definition, two parallel lines intersect at infinity.

For an arbitrary triangle ABC in Fig. 5(a), the corresponding solid angle Ω^P_{ABC} is equal to the area of the spherical triangle $A'B'C'$, which is the orthogonal projection of ABC onto the unit sphere centred at P (Van Oosterom & Strackee 1983). As depicted in Fig. 5(a), A', B' and C' are the points at which the position vectors $\vec{r}_{PA}$, $\vec{r}_{PB}$ and $\vec{r}_{PC}$, respectively, meet the surface of the sphere.

Van Oosterom & Strackee (1983) developed an efficient equation for the calculation of Ω^P_{ABC}:

$$\Omega^P_{ABC} = 2\tan^{-1}\left[\frac{\vec{r}_{PA}.(\vec{r}_{PB}\times\vec{r}_{PC})}{r_{PA}r_{PB}r_{PC}+(\vec{r}_{PA}.\vec{r}_{PB})r_{PC}+(\vec{r}_{PA}.\vec{r}_{PC})r_{PB}+(\vec{r}_{PB}.\vec{r}_{PC})r_{PA}}\right], \tag{8}$$

where r_{PA}, r_{PB} and r_{PC} are the $L2$-norms of $\vec{r}_{PA}$, $\vec{r}_{PB}$ and $\vec{r}_{PC}$, respectively. The term in the numerator, that is $\vec{r}_{PA}.(\vec{r}_{PB}\times\vec{r}_{PC})$, represents the scalar triple product of the vectors.

To calculate φ^P_{TD}, the Burgers function corresponding to any TD at an arbitrary point P, we first apply eq. (8) to calculate Ω^P_{TD}, which is the corresponding solid angle. We then use eq. (7) to calculate φ^P_{TD}. Note that for calculations based on eq. (8), the four-quadrant inverse tangent (e.g., the atan2 function in MATLAB) must be used, which accounts for the signs of the numerator and denominator of the fraction.

We now use eq. (8) to derive the equation of the solid angle and, subsequently, the Burgers function associated with an angular dislocation. For this purpose, we first replace the position vectors in eq. (8) with $r_{PA}\vec{e}_{PA}$, $r_{PB}\vec{e}_{PB}$ and $r_{PC}\vec{e}_{PC}$, where $\vec{e}_{PA}$, $\vec{e}_{PB}$ and $\vec{e}_{PC}$, respectively, are the unit vectors along the position vectors. This replacement results in an equation that is equivalent to eq. (8) but is now based only on the unit vectors:

$$\Omega^P_{ABC} = 2\tan^{-1}\left[\frac{\vec{e}_{PA}.(\vec{e}_{PB}\times\vec{e}_{PC})}{1+\vec{e}_{PA}.\vec{e}_{PB}+\vec{e}_{PA}.\vec{e}_{PC}+\vec{e}_{PB}.\vec{e}_{PC}}\right]. \tag{9}$$

As illustrated in Fig. 5(b), if the vertices B and C are shifted along the positive directions of the $\vec{e}_{AB}$ and $\vec{e}_{AC}$ vectors, respectively, to infinity, an angular dislocation is formed that originates at A. For this angular dislocation, we adopt the coordinate system convention used in Yoffe (1960), where the z-axis coincides with the AB side and the x-axis points upwards. Because B and C are already at infinity, $\vec{e}_{PB}$ and $\vec{e}_{PC}$ are parallel to the sides of the angular dislocation, and therefore, the coordinates of the unit vectors in this coordinate system are $\vec{e}_{PA} = -(x_P, y_P, z_P)/r_P$, $\vec{e}_{PB} = (0, 0, 1)$ and $\vec{e}_{PC} = (0, \sin\alpha, \cos\alpha)$. If we substitute these coordinates into eqs (9) and (7) and use the half-angle trigonometry formulae, it follows that the Burgers function at the calculation point P that corresponds to the angular dislocation with $\alpha > 0$ is

$$\varphi_A^P = \frac{1}{2\pi}\tan^{-1}\left[\frac{x_P}{(r_P - z_P)\cot(\alpha/2) - y_P}\right]. \tag{10}$$

Negating the numerator and the denominator of eq. (10) while using the four-quadrant tangent function also enables calculations for values of $\alpha < 0$.

The partial derivatives of this function with respect to x, y and z are

$$\begin{aligned}
\frac{\partial\varphi_A^P}{\partial x} &= \frac{1}{4\pi}\left[\frac{\eta_p}{r_P(r_P - \zeta_P)} - \frac{y_p}{r_P(r_P - z_P)}\right]\\
\frac{\partial\varphi_A^P}{\partial y} &= \frac{1}{4\pi}\left[\frac{x_p}{r_P(r_P - z_P)} - \frac{x_p\cos\alpha}{r_P(r_P - \zeta_P)}\right]\\
\frac{\partial\varphi_A^P}{\partial z} &= \frac{1}{4\pi}\frac{x_p\sin\alpha}{r_P(r_P - \zeta_P)},
\end{aligned} \tag{11}$$

where $\zeta_P = y_P\sin\alpha + z_P\cos\alpha$.

All partial derivatives in eq. (11) are identical to those given by Yoffe (1960). Because the Burgers function does not include any constant term (see eq. 10), the equality of the partial derivatives verifies eq. (8) and guarantees the validity of our approach.

These equations contain only one arc-tangent term, which makes them very efficient to calculate. Moreover, eq. (10) remains single-valued everywhere and also addresses the numerical instabilities of the Brown (1975) equation near $x = 0$. Below, we will use eq. (10) in our artefact-free solution for a TD in a half-space.

3 A TRIANGULAR DISLOCATION IN A HALF-SPACE

In many geophysical applications of dislocation theory, because no stress is transferred from the solid earth to the atmosphere, the Earth's surface is simulated as a free surface (Segall 2010).

Following Jeyakumaran *et al.* (1992) and Meade (2007) and using the coordinate transformation scheme presented in Section 2.1, we now develop a general solution for a triangular dislocation (TD) in a half-space. We use this general solution merely to calculate the effect of a free surface on a TD and then develop an artefact-free solution in a half-space by using the method of images.

3.1 The general solution for a TD in a half-space

3.1.1 The structure of the solution

By applying the method of images to the Yoffe (1960) solution in a full-space, Comninou & Dundurs (1975) developed the mathematical equations associated with an angular dislocation in a half-space that are applied for displacement calculations at the surface and at depth as well as calculations of the strain and rotation tensor at the surface only. The solution was developed for an angular dislocation with a vertical leg (perpendicular to the surface) and an angle that is restricted to the interval $[-\pi/2, \pi/2]$, as shown in Fig. 6. Therefore, the dislocation lines of the angular dislocation never intersect the surface, unless the origin is located at the surface and the angle is exactly $\pm\pi/2$. The equations in Comninou & Dundurs (1975) are given in the ADCS, which is detailed in Section 2.1 and is shown as the $y_1y_2y_3$ coordinate system in Fig. 6. The y_1, y_2 and y_3 axes of this figure correspond to the y-, x- and z-axes, respectively, that are used by Yoffe (1960).

The solution for the angular dislocation in a half-space consists of three parts: the main dislocation, the image dislocation and a harmonic function (Comninou & Dundurs 1975). The image dislocation, which is the mirror image of the main dislocation with respect to the free surface, cancels the surface shear traction of the main dislocation but doubles the surface normal traction. The harmonic function eliminates the resultant surface normal traction to fulfil the zero-traction boundary condition at the free surface (Comninou & Dundurs 1975). Therefore, the half-space solutions for the displacement vector $\vec{d}$ and the stress tensor S can be written as follows:

$$\vec{d} = \vec{d}^{\,MD} + \vec{d}^{\,ID} + \vec{d}^{\,HF}, \tag{12}$$

$$S = S^{MD} + S^{ID} + S^{HF}. \tag{13}$$

The superscripts *MD*, *ID* and *HF* of the terms on the right-hand sides of eqs (12) and (13) represent the contributions of the main dislocation, the image dislocation and the harmonic function, respectively. To calculate the contributions of the main and image dislocations, the full-space

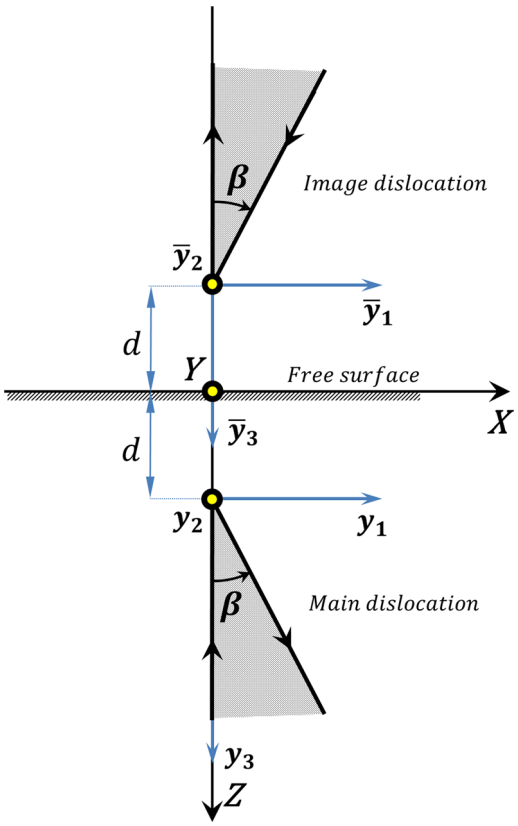

Figure 6. Half-space formulation of an angular dislocation, composed of the main dislocation, the image dislocation and a harmonic potential function (Comninou & Dundurs 1975). The image dislocation (here, the dislocation on the upper side) is the mirror image of the main dislocation (here, the dislocation on the lower side), whose origin is located at a depth d. All coordinate systems shown here are right-handed, and the y_2, $\bar{y}_2$ and Y-axes, which are shown as black-and-yellow circles, are normal to the plane and point outwards. Following the convention of Comninou & Dundurs (1975), in this figure, the positive direction of the Z-axis points downwards and $Z = 0$ defines the free surface. The half-space equations give the displacements and stresses in terms of $y_1y_2y_3$, which is the main dislocation coordinate system.

solution detailed in Appendix B must be used, whereas the contributions of the harmonic function to eqs (12) and (13) are given by Comninou & Dundurs (1975) and Meade (2007), respectively.

A solution for a TD in a half-space was developed by Jeyakumaran *et al.* (1992) through the superposition of six angular dislocations in the half-space. The complete strain equations along with the details of the method used to construct the solution in the half-space are given by Meade (2007).

Here, we first follow the same approach used in these earlier studies and combine it with the coordinate transformation approach (Appendix A). In this manner, we develop a general solution for a TD in a half-space with the configuration depicted in Fig. 7. In our conventions, the EFCS is defined with the positive Z-axis pointing upwards. Therefore, the vertices of the TD in the half-space have Z components that are negative or, in case that the free surface is reached, zero. The procedure for the calculations associated with a TD in a half-space is summarized in the diagram presented in Fig. 8. When considering the new ADCS in the half-space, we simply use the direct transformation between the EFCS and the ADCS. However, we transform the slip vector from the TDCS into the EFCS and then from the EFCS into the ADCS of each angular dislocation. Thus, the EFCS plays the role of both an intermediate and the final coordinate system.

3.1.2 The implementation procedure

To construct the transformation matrices, we first calculate the strike, dip and normal to the TD vectors, using the right-hand rule for vertex ordering. Therefore, the transformation matrix of eq. (1) can be used for direct transformation from the TDCS into the EFCS. The details regarding the calculation of the components of this transformation are presented in Section 2.1. Now, using A_{TE} in eq. (A3), we can transform the slip vector from the TDCS into the EFCS.

The transformation matrices $A_{AE_1}, \ldots, A_{AE_6}$ for the direct transformation from each ADCS into the EFCS consist of the coordinates of $\{\vec{e}^k_{y_1}, \vec{e}^k_{y_2}, \vec{e}^k_{y_3}\}$ for $k = 1, 2, \ldots, 6$, which are the unit vectors along the axes of the ADCS that correspond to each of the six angular dislocations. It can be observed in Fig. 7 that along each side of the TD in the half-space, there is a pair of coplanar angular dislocations whose origins are located at the vertices of that side of the TD. These two angular dislocations have the same angles but opposite slip vectors (Fig. 9a). The ADCSs of these two angular dislocations have parallel axes, and their y_1-axis is parallel to the projection of the corresponding side of the TD onto the free surface. Considering the TD depicted in Fig. 7, if we represent the coordinates of P_1, P_2 and P_3 in the EFCS

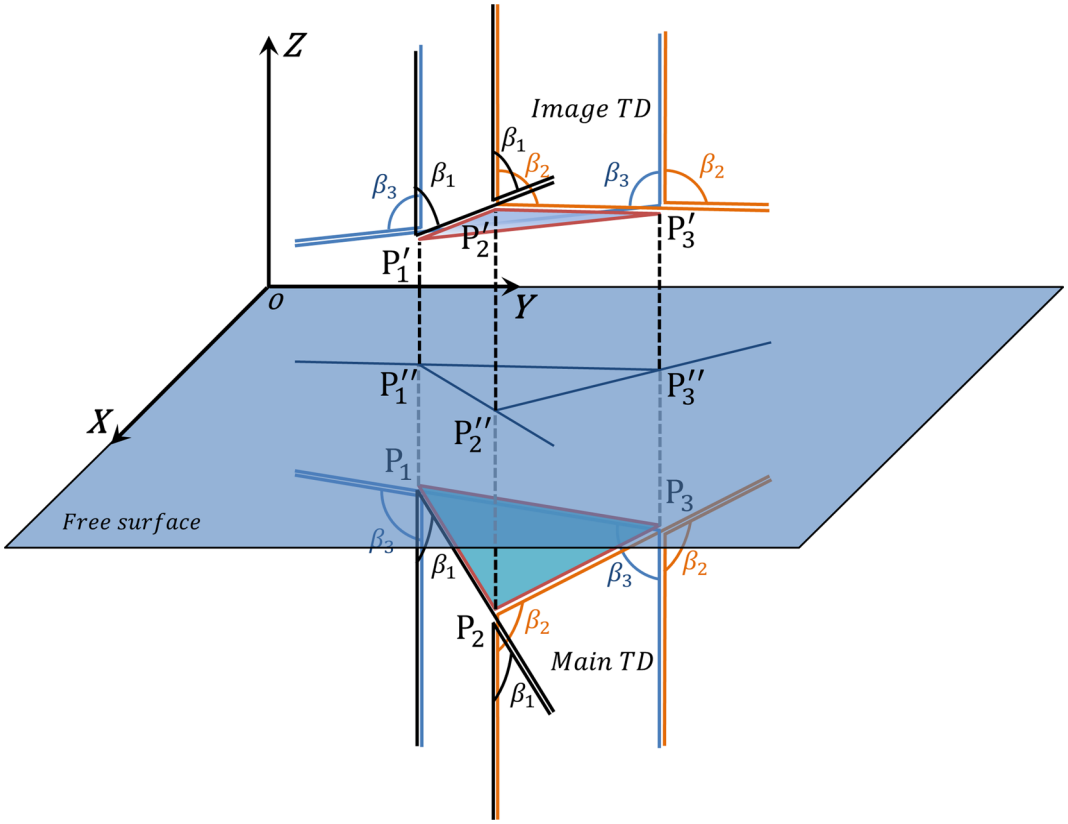

Figure 7. Half-space formulation of a triangular dislocation (TD), modified from Jeyakumaran *et al.* (1992). The triangles $P_1P_2P_3$ and $P_1'P_2'P_3'$ are the main and image TDs, respectively, and $P_1''P_2''P_3''$ is their projection onto the free surface. The solid lines connected to P_1, P_2 and P_3 form the first set of artefact singularities, and the other solid lines, connected to P_1'', P_2'' and P_3'', form the second set of artefact singularities discussed in Section 3.2. These artefact singularities affect the displacements, strains and stresses. The vertical dashed lines indicate the locations of the artefact singularities, which affect the strains and stresses only.

as $r_{P_1} = (X_{P_1}\ Y_{P_1}\ Z_{P_1})^T$, $r_{P_2} = (X_{P_2}\ Y_{P_2}\ Z_{P_2})^T$ and $r_{P_3} = (X_{P_3}\ Y_{P_3}\ Z_{P_3})^T$, respectively, then the coordinates of their respective projections onto the free surface, P_1'', P_2'' and P_3'', will be $r''_{P_1} = (X_{P_1}\ Y_{P_1}\ 0)^T$, $r''_{P_2} = (X_{P_2}\ Y_{P_2}\ 0)^T$ and $r''_{P_3} = (X_{P_3}\ Y_{P_3}\ 0)^T$. As a result, the unit vectors $\vec{e}^{\,k}_{y_1}$ for $k = 1, 2, \ldots, 6$, which are the unit vectors along the projections of P_1P_2, P_2P_3 and P_3P_1, are $\vec{e}^{\,1}_{y_1} = \vec{e}^{\,2}_{y_1} = (\vec{r}''_{P_2} - \vec{r}''_{P_1})/\|\vec{r}''_{P_2} - \vec{r}''_{P1}\|$, $\vec{e}^{\,3}_{y_1} = \vec{e}^{\,4}_{y_1} = (\vec{r}''_{P_3} - \vec{r}''_{P_2})/\|\vec{r}''_{P_3} - \vec{r}''_{P_2}\|$ and $\vec{e}^{\,5}_{y_1} = \vec{e}^{\,6}_{y_1} = (\vec{r}''_{P_1} - \vec{r}''_{P_3})/\|\vec{r}''_{P_1} - \vec{r}''_{P_3}\|$. We number the angular dislocations along the P_1P_2 side with the vertices P_1 and P_2 as their origins as the first and second angular dislocations, respectively. The third and fourth angular dislocations are those along the P_2P_3 side with the vertices P_2 and P_3, respectively, as their origins. Finally, the fifth and sixth angular dislocations are those along the P_3P_1 side with the vertices P_3 and P_1, respectively, as their origins. However, $e^k_{y_3} = (0\ \ 0\ \ -1)^T$ clearly holds because these unit vectors are oriented along the vertical legs of the angular dislocations and point downwards. Because the $y_1y_2y_3$ coordinate system is right-handed, it also holds that $\vec{e}^{\,k}_{y_2} = \vec{e}^{\,k}_{y_3} \times \vec{e}^{\,k}_{y_1}$, which completes the construction of the required transformation matrices. Starting from the coordinates of the TD vertices in the EFCS and using $A_{AE1}, \ldots, A_{AE6}$ in eqs (A4) and (A6), we can transform the coordinates of the slip vector and the calculation points from the EFCS into each ADCS. The angles of the six angular dislocations can be calculated using $\beta_1 = \cos^{-1}(-\vec{e}_{12}.\vec{e}_Z)$, $\beta_2 = \cos^{-1}(-\vec{e}_{23}.\vec{e}_Z)$ and $\beta_3 = \cos^{-1}(-\vec{e}_{13}.\vec{e}_Z)$, where $\vec{e}_{12} = (\vec{r}_{P_2} - \vec{r}_{P_1})/\|\vec{r}_{P_2} - \vec{r}_{P_1}\|$, $\vec{e}_{13} = (\vec{r}_{P_3} - \vec{r}_{P_1})/\|\vec{r}_{P_3} - \vec{r}_{P_1}\|$ and $\vec{e}_{23} = (\vec{r}_{P_3} - \vec{r}_{P_2})/\|\vec{r}_{P_3} - \vec{r}_{P_2}\|$ are the unit vectors along the sides of the TD.

To calculate the final results, the contribution of each angular dislocation to the displacements and the stresses must first be transformed into the EFCS. Superposition of the individual contributions yields the final results.

3.2 Developing an artefact-free solution for a TD in a half-space

With regard to the geometry and configuration of the angular dislocations in the half-space solution presented in Figs 6 and 7, we find that the results are subject to even more artefact singularities than the full-space solution. In this case, in addition to those on the extensions of the sides of the TD, additional artefact singularities are present beneath and above the vertices of the TD. These artefact singularities are indicated by the solid and dashed lines around the TD in Fig. 7. The first set of solid lines represents the slant and vertical legs of the main angular dislocations, which cause problems similar to those encountered in the full-space case. The second set of solid lines constitutes those at the free surface, representing the harmonic function, which eliminates the normal traction of the free surface. The artefact singularities on

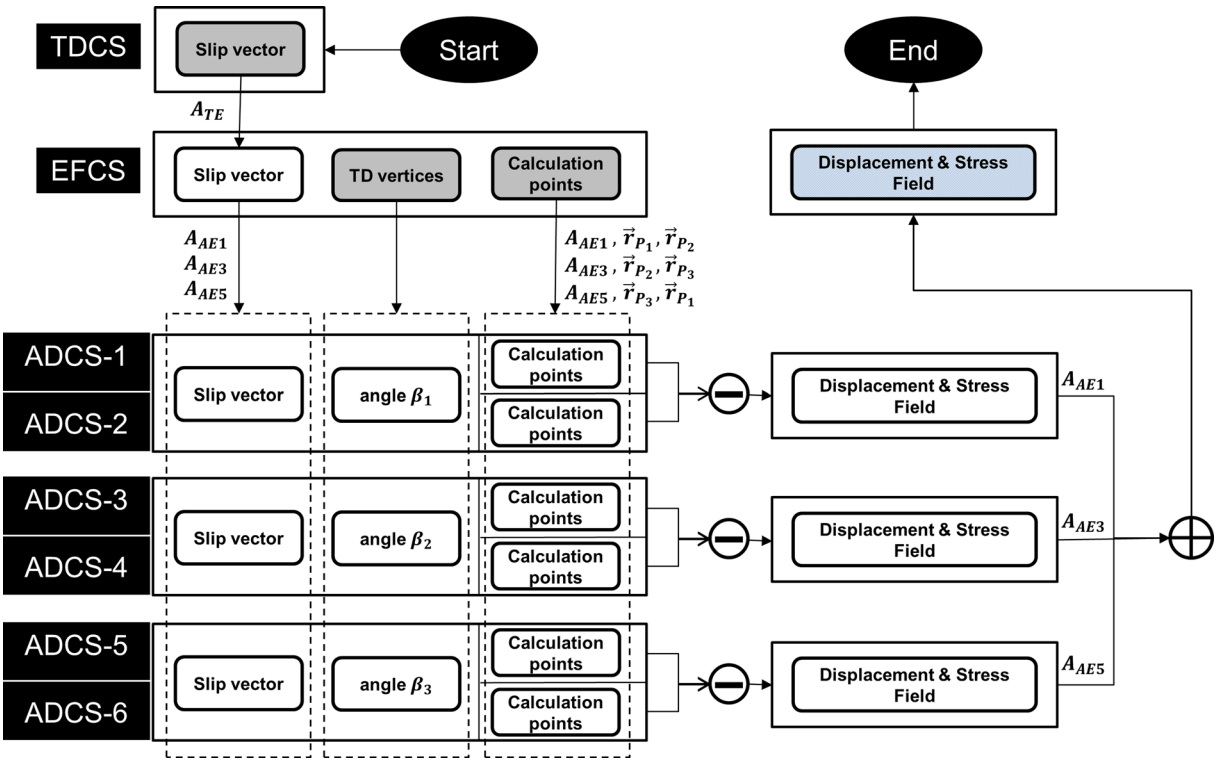

Figure 8. Flowchart for calculating the displacement and stress field of a triangular dislocation (TD) in an Earth-fixed coordinate system (EFCS) in a half-space. The first box on the left side of each row indicates the coordinate system corresponding to the other boxes in that row. The grey boxes represent the inputs, and the blue box represents the final output. The coordinates of the slip vector in the triangular dislocation coordinate system (TDCS) are first transformed into the EFCS (see eq. A3 in Appendix A). The coordinates of the calculation points and the TD vertices are then transformed from the EFCS into each of the six angular dislocation coordinate systems (ADCSs; see eqs A9 and A5 in Appendix A). After the contribution of each angular dislocation is calculated, the results are transformed into the EFCS (see eqs A4 and A10 in Appendix A). The superposition of the individual contributions of the angular dislocations yields the final result.

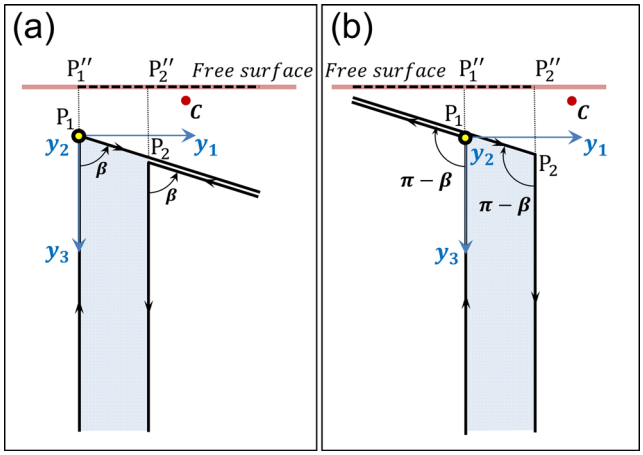

Figure 9. Two equivalent configurations associated with the pair of angular dislocations along the side P_1P_2. The dashed line along $P_1''P_2''$ is the projection of the dislocation lines onto the free surface. Here, $y_1y_2y_3$ is the angular dislocation coordinate system (ADCS) of the angular dislocation at P_1. The configuration depicted in (a) is used for points with negative y_1 coordinates, and the configuration depicted in (b) is used for points with positive y_1 coordinates. For points such as C, we avoid the artefacts along the dashed lines by using this technique to calculate the contribution of the harmonic function in our artefact-free half-space solution.

these lines and the numerical instabilities in their vicinity emerge whenever at least one of the sides of the main TD intersects the free surface or when the dislocation is very shallow. The vertical dashed lines above the TD vertices represent the artefact singularities arising from the miscalculation of the Burgers function or its partial derivatives.

We develop an artefact-free solution in a half-space by applying the method of images directly to the TDs (Fig. 7). We note that the final result of the superposition of the six TDs in the half-space can also be written in the form of eqs (12) and (13). In this case, the first and second terms represent the contributions of the main and image TDs, respectively, which are shown in Fig. 7 as $P_1P_2P_3$ and $P_1'P_2'P_3'$, respectively.

The third term expresses the contribution of the harmonic function associated with the main and image TDs and is virtually represented by $P_1'' P_2'' P_3''$ in Fig. 7. Accordingly, we propose our artefact-free solution in a half-space in two steps. In step 1, we calculate the artefact-free contributions of the main and image TDs. In step 2, we calculate the artefact-free contribution of the harmonic function to the displacements and stresses that correspond to the TD. The superposition of the outputs of these two steps yields the final results.

3.2.1 Step 1

In step 1, we use the same EFCS in which the positive Z-axis points upwards and $Z = 0$ represents the free surface. We calculate the contribution of the main and image TDs using the full-space artefact-free solution that we developed in Section 2.2. The horizontal coordinates of the vertices of the main and image TDs in the EFCS are the same, whereas the values of their vertical components are additive inverses. Therefore, to obtain consistent results, with the exception of the Z coordinates of the vertices, which are opposite, we consider the same input parameters for the main and image TDs, including the same vertex ordering and the same slip vectors. According to this model framework and the conventions that we adopted for the TDCS, the strike vectors of the main and image TDs have parallel but opposite directions. However, our convention for a completely horizontal TD produces the same strike vectors for both the main and image TDs. We correct for this exceptional case by negating the components of the strike vector for the image TD after calculating the normal vector. The dip vector is then calculated as the cross product of the normal and strike vectors.

Now, we calculate the contributions of the main and image dislocations using our artefact-free solution for a TD in a full-space. Consequently, the artefact singularities along the first set of solid lines and the dashed lines will no longer exist in the model.

3.2.2 Step 2

In step 2, we recall from Section 3.1.1 that $\vec{d}^{\,HF}$ and S^{HF} are the contributions of the harmonic function to the displacement and stress fields, respectively, of an angular dislocation in a half-space. Now, we calculate the contributions of the harmonic function to the displacements and stresses associated with a TD in a half-space by applying the technique discussed in Section 3.1, only now we apply it to the $\vec{d}^{\,HF}$ and S^{HF} terms in eqs (12) and (13). However, this calculation is still subject to the artefacts represented by the solid lines on the free surface in Fig. 7, as discussed before. These lines are the projections of the plunging legs of the pairs of angular dislocations along the sides of the main TD. The two configurations represented in Fig. 9 can be used equivalently to calculate the contribution of each pair of angular dislocations along each side of the TD in the half-space. Note that to use the second alternative in Fig. 9, the angle β must be replaced by the opposite of its supplementary angle, $\beta - \pi$, while the other inputs remain unchanged. According to Fig. 9, for the calculation points, which have positive y_1 coordinates, we must use the alternative configuration in Fig. 9(b), whose artefacts extend along the negative y_1 axis, and vice versa. In this manner, we can always avoid the artefacts on the free surface.

Superposing the outputs of Sections 3.2.1 and 3.2.2 produces the final solution for a TD in a half-space, which is free from all the various artefacts that we discussed before.

4 VALIDATION OF THE NEW ARTEFACT-FREE SOLUTIONS

With regard to the lengthy equations associated with a TD in either a full-space or half-space and with regard to the procedure that we applied to address the artefacts in these equations, analytical verification of our method is not feasible. One approximate method of verification consists of comparing the results to those of the available numerical methods for dislocation model calculations (Jeyakumaran *et al.* 1992). However, the absolute precision of the solution may arguably remain unresolved in this case. A superior alternative applied in other, earlier works by Thomas (1993) and Meade (2007) is to validate the solution using the analytical solution for an RD in a half-space, as summarized by Okada (1992).

Here, we first compare our solution for a TD in a half-space to the solution of Meade (2007). The purpose of this comparison is to validate our solution for the regular calculation points, those that do not lie near the artefact singularities. This comparison also demonstrates the ability of our method to address the artefacts. For this purpose, we consider the TD and calculation points shown in Fig. 10. The coordinates and the first components of the displacement vector and strain tensor that correspond to the calculation points are listed in Table 3. The first three points, which form a line parallel to the Z-axis, are located at the centroid of the TD, above it, and underneath it. The next six points are located on the extensions of the sides of the TD, and the remaining six lie above or underneath the vertices.

In Table 3, the results of our method are presented as u and ϵ_{XX}, which represent the first displacement component and the first strain component, respectively; the corresponding outputs obtained using the Meade (2007) code are presented as u' and ϵ'_{XX}. For the calculations, we consider a Poisson's ratio of 0.25. The coordinates of the vertices of the TD are $(-1, -1, -5)$, $(1, -1, -5)$ and $(-1, 1, -4)$. In our calculations, the coordinates of the TD vertices and the coordinates of the calculation points share the same unit of length, which may be any unit that is desired. The components of the TD slip vector, which correspond to the strike slip, the dip slip and the opening, are 1, -1 and 2, respectively. The components of the TD slip vector and of the displacement vector also share the same arbitrary unit.

The calculated displacements and strains for points No. 1, No. 2 and No. 3 in Table 3 demonstrate that the results of our method compare very well with the outputs of the Meade (2007) code. The differences of less than 10^{-15} indicate excellent agreement between the two approaches for calculation points far from the artefact singularities.

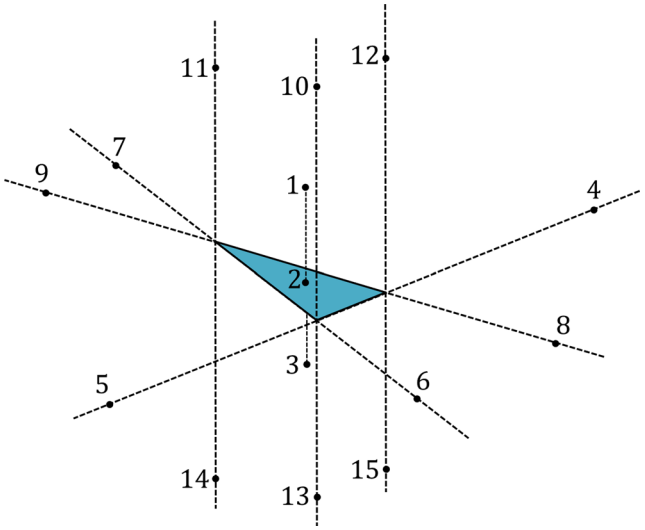

Figure 10. The triangular dislocation (TD) in a half-space and the calculation points on the artefact singularities that are used for the validation and comparison of the results of our method with respect to the Meade (2007) solution.

Table 3. The coordinates, displacements and strains corresponding to the points shown in Fig. 10. The 'NaN' values and the grey fields in the table indicate the artefact singularities and numerical instabilities in the Meade (2007) code. Note that our approach allows for valid computation of these points. For the first three points, both approaches retrieve the same results, demonstrating the correctness of both methods at calculation points that are not subject to artefact singularities.

#	X	Y	Z	u (This paper)	u' (Meade 2007)	ϵ_{XX} (This paper)	ϵ'_{XX} (Meade 2007)
1	−1/3	−1/3	−3	0.0352311877319734	0.0352311877319732	0.0481047005255181	0.0481047005255181
2	−1/3	−1/3	−14/3	−0.509465745232405	−0.509465745232405	−0.244188978214975	−0.244188978214977
3	−1/3	−1/3	−6	−0.0450664903903138	−0.0450664903903139	0.0546831404832553	0.0546831404832554
4	7	−1	−5	−0.00230579292792908	NaN	0.000829157341339727	NaN
5	−7	−1	−5	0.00401472894583963	0.00401472894583941	0.00114439668841158	NaN
6	−1	−3	−6	0.00483219740842196	NaN	−0.00386292388925956	NaN
7	−1	3	−3	0.00261498816660580	0.00261498816660530	−0.00243788640223540	NaN
8	3	−3	−6	−0.00498017723062124	0.0498371783469113	0.000706397690338731	142952905402461
9	−3	3	−3	0.00469791958297159	0.00469791958297180	0.000211254167350266	0.00431126958717604
10	−1	−1	−1	0.00147786823004841	0.00147786823004838	0.00650800501584133	NaN
11	−1	1	−1	0.00374844575688324	0.447846746319388	0.000922452413344460	NaN
12	1	−1	−1	0.0166558386729541	−0.427442461889551	0.00441202690885827	NaN
13	−1	−1	−8	−0.00656347406353817	NaN	0.00330232019558791	NaN
14	−1	1	−8	−0.0105680479573571	NaN	0.00876398663844928	NaN
15	1	−1	−8	−0.00213929091658054	NaN	−0.000914111766849476	NaN

As another reference for the validation of our method, we use the solution of Okada (1992) for an RD. We construct the displacement field of an RD by superposing the displacements of two TDs in a half-space that form exactly the same RD (Fig. 11a; see also Meade 2007). We use the same conventions for the units of the various quantities as those used in the first part of this section. The midpoint of the upper edge of the RD is located at a depth of two beneath the origin of the EFCS. The RD has a dip angle of 30°, a strike angle of 10°, and a length and width of 1.5 and 0.75, respectively. We consider a unit slip vector with a rake angle of 90° on the RD and calculate the corresponding displacements on a 2 × 2 grid beneath the RD, centred on the origin of the EFCS. The approximate coordinates of the vertices of the RD are $P_1(0.1302, 0.7386, -2.0000)$, $P_2(-0.1302, -0.7386, -2.0000)$, $P_3(0.5094, -0.8514, -2.3750)$ and $P_4(0.7699, 0.6258, -2.3750)$. The precise coordinates can be calculated using the RD parameters that we specified earlier. As shown in Fig. 11(a), $P_1P_2P_3$ and $P_3P_4P_1$ are the two TDs that, together, are geometrically equivalent to the RD. These TDs share the same slip vector, $(0, 1, 0)$. We calculate and superpose the displacements of the TDs on the same grid using our artefact-free solution for the two TDs in the half-space. The displacements of the TDs and the RD, as well as the differences between the two, are illustrated in Fig. 11. The results are comparable, and the differences are on the order of 10^{-15}. The same order of accuracy has been reported by Meade (2007) for various calculation points at the surface.

As we have used our artefact-free solution for a TD in a full-space to develop the artefact-free solution in a half-space, the presented validation test can be regarded as a simultaneous verification of the artefact-free solutions in both full-space and half-space. All results presented and discussed here can be reproduced using our MATLAB codes, which accompany this paper.

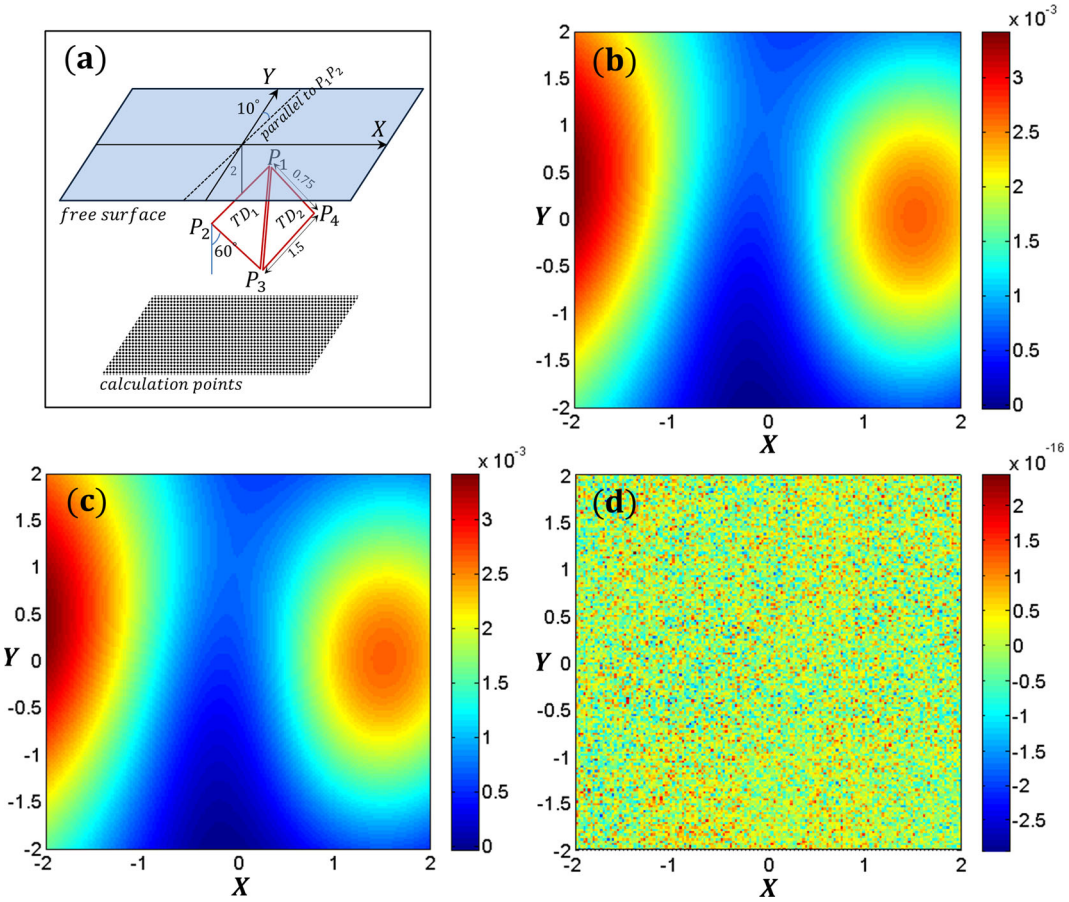

Figure 11. The validation of our approach against the Okada (1992) solution by superposing two triangular dislocations to construct a rectangular dislocation in a half-space with a slip vector of (0, 1, 0). (a) The model set-up. (b) The first component of the displacements on the grid shown in panel (a), calculated using our method. (c) The first component of the displacements on the calculation points, calculated using the Okada (1992) method. (d) The differences between (b) and (c). The X and Y coordinates have the same unit as the dislocation dimensions. The colour bars indicate the calculated displacements, which have the same unit as the slip vector components (see Section 4).

5 DISCUSSION

In this paper, we developed fully analytical, artefact-free solutions for a TD in a full-space and half-space. Our solution in a full-space consists of two equivalent configurations of three angular dislocations (Yoffe 1960). Each of these configurations is free of any artefact singularities in its domain of definition. These domains of definition are complementary, that is they cover the entire $\mathbb{R}^3$ space. We also replaced the Burgers function equation in Yoffe (1960) with a more efficient equation based on Van Oosterom & Strackee (1983). This new equation, which we verified analytically, also addresses the problem of the Burgers function producing multiple outputs for a single input (Brown 1975). Using this new full-space solution in the method of images, along with the harmonic function given by Comninou & Dundurs (1975), we developed a new artefact-free solution in a half-space. There is no rigid-body motion associated with our half-space solution because of the new configurations of the superposed angular dislocations.

5.1 Limitations of the method

The solutions that we developed for TDs in this paper are Volterra dislocations (Volterra 1907). Therefore, a general disadvantage of our solution is that it can only account for a uniform slip on each TD surface. In other words, no variation in the slip on the surface of a single TD is allowed. As a result, because of the existing discontinuity of the slip vector components at the dislocation boundaries, the stresses there become unbounded. This may be inconvenient when calculating the displacements and stresses in the near field, for example, when considering the crack tip in a crack propagation problem. As a rule of thumb, the average length of the TD sides can be regarded as the characteristic distance that should exist between the calculation points and the dislocation boundaries to obtain accurate results (Crouch & Starfield 1983). However, this rule does not apply to the centroid of the TD, for which the results are absolutely valid. Developing analytical solutions that allow for slip variations on the dislocation surface as a linear function, for example, can address the problem.

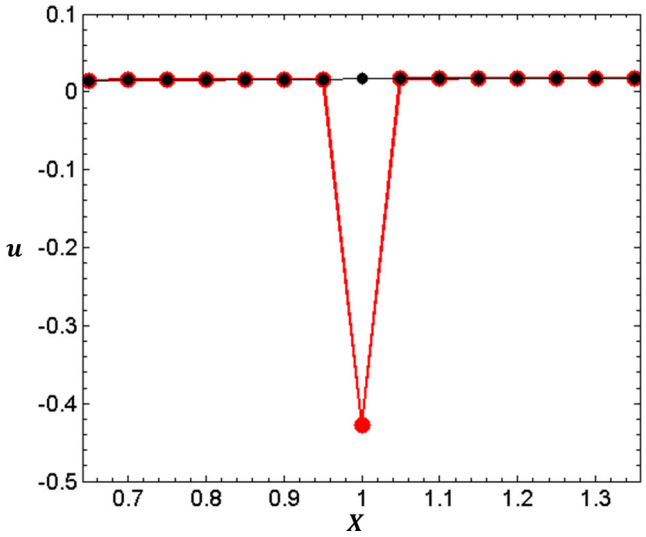

Figure 12. The discontinuity in the first component of the displacement (***u***) along the *X*-axis in the neighbourhood of point No. 12 above one of the vertices of the triangular dislocation (TD) depicted in Fig. 10 caused by the miscalculation of the Burgers function. The black line shows the results of our code, and the red curve shows the output of the Meade (2007) code. The axes may have any arbitrary units of length (see Section 4).

In the development of the MATLAB codes, we frequently used the vectorization technique, thus making the codes highly optimized for ordinary desktop computers. However, these vectorization techniques are not supported by the parallel calculation functionalities of MATLAB. Therefore, the current version of our codes is not suited to parallel calculations in MATLAB on computers with multicore CPUs.

5.2 Improvements on and comparison to earlier works

The previous analytical solutions for the TD case, as mentioned above, are subject to various artefact singularities. The Yoffe (1960) approach, which was the first solution for TDs in a full-space and is detailed in Section 2.1, exhibits artefact singularities on the extensions of the sides of the TD, as shown in Fig. 3. The other shortcoming of the Yoffe (1960) approach is related to the Burgers function producing multiple outputs at a single calculation point, as first considered by Brown (1975). Crouch & Starfield (1983) developed an alternate solution for a TD in a full-space, which was later utilized in a BEM implementation developed by Kuriyama & Mizuta (1993). The latter also reported the existence of singularities on the extensions of the sides of the TD, which is considered to be a major shortcoming of the method.

Jeyakumaran *et al.* (1992) developed the first solution for a TD in a half-space using the method detailed in Section 3.1. Nonetheless, as discussed in Section 3.2, the solution of Jeyakumaran *et al.* (1992) possesses new artefact singularities below and above the vertices of the TD, in addition to those present in the Yoffe (1960) full-space solution (Fig. 7). Thomas (1993) developed Poly3D, which is a BEM implementation written in the C programming language and is based on the Jeyakumaran *et al.* (1992) method. Using the geometric method elaborated on here in Section 3.2.2, Poly3D removes the artefact singularities on the extensions of the sides of the TD. However, the singularities below and above the vertices still remain. Meade (2007) also implemented the Jeyakumaran *et al.* (1992) approach using MATLAB and elaborated the method in greater detail. Although the Meade (2007) approach exhibits considerably higher accuracy than the Thomas (1993) outputs, none of the artefact singularities are addressed. To illustrate the effect of these singularities on the calculations, we recall the results of the validation test presented in Section 4 (see Table 3 and Fig. 10).

Comparing the displacements first, we find differences of less than 10^{-15} for the first three points (No. 1, No. 2 and No. 3), thus observing excellent agreement between the two methods. This is because these points are far from any artefact singularities. The singular results in the Meade (2007) outputs are represented by 'NaN', which stands for 'Not a Number'. We observe artefact singularities for all points underneath the vertices of the TD as well as along the downwards-dipping extensions of the TD sides. Because of the limited accuracy of the values stored in the computer, the point No. 8 in the Meade (2007) code is considered to be located not on the downwards-dipping line of the artefact singularity but merely in its vicinity. Therefore, the Meade (2007) approach produces an incorrect output that exhibits the numerical instability discussed in Section 3. Finally, we observe incorrect displacements for points No. 11 and No. 12, which are above the vertices of the TD. Although there are no artefact singularities near points No. 11 and No. 12, the miscalculation of the Burgers function in the Meade (2007) code results in a discontinuity in the displacements. This discontinuity is more apparent in Fig. 12, where we show the first component of the displacement vector in the neighbourhood of point No. 12.

When considering the calculated strains, for the first three points (No. 1, No. 2 and No. 3), we also detect differences of less than 10^{-15}. Nevertheless, for the remainder of the calculation points, apart from points No. 8 and No. 9, which exhibit large numerical instabilities, the output of the Meade (2007) code is 'NaN', reflecting the singularity of the calculations. This is partially attributable to the artefact singularities beneath the vertices and along the downwards-dipping extensions of the TD sides. For the remaining calculation points, however,

the singularity of the strain calculations is caused by the use of inappropriate partial derivatives of the Burgers function rather than eq. (11). Apart from the artefact singularities discussed here, the results of our code and those of the Meade (2007) code at any other calculation point in a half-space exhibit perfect agreement on the order of 10^{-15}, which is the accuracy of double-precision numbers near unity in MATLAB.

Gimbutas *et al.* (2012) applied a combination of analytical and numerical quadratures to the Green's function for full-space (Kelvin 1848) and half-space (Mindlin 1936) point sources to develop the corresponding solutions as well as corresponding FORTRAN codes for a TD in a full-space and half-space. To address the problem of artefact singularities in a full-space, Gimbutas *et al.* (2012) approximated the solution using a Taylor series expansion inside the cones that encircle the extension of each TD side. These cones have a vertex angle of 2×10^{-8} rad, and their origins are the TD vertices (Gimbutas *et al.* 2012). Similar to other solutions based on numerical quadrature schemes, the presence of a fixed number for the vertex angle serves as a threshold for this approach and results in scale-dependent outputs. To remove the artefact singularities and obtain the half-space solution, a fully numerical adaptive quadrature rule for calculating the image dislocation and the contribution of the potential function is applied (Gimbutas *et al.* 2012). This technique, although it offers certain advantages, yields low-quality results for calculation points and TDs near the free surface where the main and image dislocations are very close to each other. In particular, the calculations at the centroid of a TD that lies at the free surface become either singular or ill-posed.

The artefact-free solutions for a TD in a full-space and half-space that we developed in this paper are fully analytical, and no approximations or series expansion methods are applied in our approach. Consequently, our solutions are independent of the units of the input parameters, and the accuracy of the results, as discussed in Section 4, is on the order of 10^{-15}, equivalent to the accuracy of double-precision values for numbers near unity. By reducing the number of arc-tangent terms present in the equations that we used for the calculation of the Burgers function in the displacement calculations, we addressed the problem of multivaluedness in the displacements. Moreover, we modified the equations in accordance with the effect of the free surface presented in Meade (2007) by manually grouping similar terms in the equations. We also used eq. (10) for the calculation of the contributions of the Burgers function to these equations. As a result, these equations became much less complex, and we thereby reduced the time required for large calculations by a factor of three. We developed optimized MATLAB codes to calculate the displacement, strain and stress fields associated with a TD in a full-space and half-space. These codes are available in the Supporting Information of this paper.

5.3 Application possibilities

Our solutions can be applied to a wide range of problems in modelling, including nano- and microfracturing and dislocations in engineering and physics as well as geological faults with an extent of several tens of kilometres. This wide range of applicability is because of the fully analytical approach that we used and also the scale-independent techniques that we developed for the removal of the artefact singularities. Our approach also allows for the use of complex meshes of any size for the TDs and can thus be used for the simulation of any curved surface in various disciplines. Our solutions can be used as the basis for other numerical methods, such as the BEM, which utilize TDs as fundamental elements. Inverting the coseismic surface deformation for the slip on complex curved faults associated with earthquakes (Maerten *et al.* 2005), analysing the deformations and stress fields of volcanoes arising from fractures and pressurized reservoirs underneath realistic edifice topographies (Cayol & Cornet 1997), and evaluating the excavation-induced displacements and stresses near man-made cavities (Kuriyama & Mizuta 1993) are a few examples of the possible applications of this approach.

5.4 Implications and further work

TDs have the advantage that they can be used to simulate sources with complex geometries, such as reservoirs, cavities and curved fault zones, without leaving any discontinuities in the model. Considering the high performance of computational facilities that are available even on desktop computers and the availability of high-resolution observation techniques, the need for more sophisticated and more accurate modelling methods that can integrate many TDs is emerging more strongly than before. The ability to achieve quality calculations in such models is guaranteed by the application of our solutions, first, because the calculations involved in our solutions are not affected by the previously discussed artefact singularities and numerical instabilities (see Sections 2 and 3), and second, because our solutions are independent of the scale of the model parameters, including the number and size of the TDs in a model. Therefore, especially for high-resolution models, our solutions strongly improve model handling and results.

In this work, we addressed only the problem of artefact singularities for a Volterra-type TD. For a more realistic simulation of natural processes, however, the intrinsic singularities at the edges of the TDs should also be taken into consideration, because these singularities result in infinite stresses accumulated at a single point in models, which are unlikely to arise in nature. Considering earlier attempts to remove these intrinsic singularities, since the 1960s, Cai *et al.* (2006) developed a non-singular analytical solution for the stress field of a straight segment dislocation in a full-space. For this purpose, the Burgers vector, which, in the classical definition of Volterra (1907), is concentrated at the points of a dislocation line, is given a new definition in which it is isotropically spread about every point within a certain spreading radius (Cai *et al.* 2006). In general, it is possible to use segment dislocations to construct a TD (Hirth & Lothe 1982). Therefore, the segment solution of Cai *et al.* (2006) can also be used to develop a singularity-free solution for a TD in a full-space. However, because Cai *et al.* (2006) provided only the stress equations, the displacement equations would first need to be determined. Using these equations along with the coordinate transformation scheme (see Appendix A) and the contributions of the Burgers function (see Section 2.3), the development of such

a solution seems straightforward. However, reasonable values for the spreading function that corresponds to the Cai *et al.* (2006) solution and its physical interpretations in various applications, such as those in geophysics, remain to be discussed. Moreover, for the half-space solution, new equations for the harmonic potential function in accordance with the new singularity-free equations provided in Cai *et al.* (2006) also have yet to be developed.

6 CONCLUSION

Our work builds on earlier developments and addresses some of the major limitations of commonly used solutions for a TD in a full-space and half-space. We developed piecewise analytical solutions without applying any analytical or numerical approximations. Our solutions consist of two sets of equivalent closed-form equations, each of which is free of artefact singularities and numerical instabilities on one of two complementary subspaces of the entire elastic medium. Using the barycentric coordinate system, we developed simple inequalities that allow for the selection of the optimal configuration for each calculation point. The new equations for the Burgers functions associated with the angular and triangular dislocations that we presented in this paper are more computationally efficient than previous equations for this purpose.

Our solutions are fully generic and highly flexible, in the sense that they do not demand any special care with regard to artefact singularities, unique ill-posed geometries or numerical-scale dependencies. Therefore, these solutions can be applied to a variety of problems in geophysics, engineering and physics, without requiring any alterations in the units of the input data or the geometric structures of the TDs.

Based on the details of the techniques and the flowchart guidance provided here, computer codes that implement our method can be easily written in any desired programming language. We also developed highly optimized MATLAB functions that facilitate the use of our solutions in practice, making these codes very suitable for use as a basis for the development of implementations of other numerical approaches, such as the BEM, that must be run repeatedly over large data sets, especially to solve inverse problems.

The numerical validation of our solution using the widely used analytical solution for an RD in a half-space (Okada 1992) demonstrated excellent agreement between the two solutions up to the round-off error of double-precision values.

ACKNOWLEDGEMENTS

The authors appreciate various comments from Hannes Bathke, Eleonora Rivalta and Sebastian Hainzl, which improved the text. We also thank Paul Lundgren, an anonymous reviewer and the editor for their constructive comments regarding this paper. This work was supported by the European Union FP7 Marie Curie ITN, ERC project 'TOPOMOD', contract No. 264517.

REFERENCES

Bottema, O., 2008. *Topics in Elementary Geometry,* Springer Science+Business Media, LLC.

Brown, R.L.J., 1975. A dislocation approach to plate interaction, *PhD thesis,* Massachusetts Institute of Technology.

Burgers, J.M., 1939. Some considerations on the fields of stress connected with dislocations in a regular crystal lattice – I, *Proc. Koninklijke Nederlandse Akademie Van Wetenschappen,* **42,** 293–325.

Bürgmann, R., Rosen, P.A. & Fielding, E.J., 2000. Synthetic aperture radar interferometry to measure Earth's surface topography and its deformation, *Annu. Rev. Earth planet. Sci.,* **28,** 169–209.

Cai, W., Arsenlis, A., Weinberger, C.R. & Bulatov, V.V., 2006. A non-singular continuum theory of dislocations, *J. Mech. Phys. Solids,* **54**(3), 561–587.

Cayol, V. & Cornet, F.H., 1997. 3D mixed boundary elements for elastostatic deformation field analysis, *Int. J. Rock Mech. Min.,* **34**(2), 275–287.

Comninou, M. & Dundurs, J., 1975. The angular dislocation in a half space, *J. Elasticity,* **5**(3–4), 203–216.

Coxeter, H.S.M., 1969. *Introduction to Geometry,* John Wiley & Sons, Inc.

Crouch, S.L. & Starfield, A.M., 1983. *Boundary Element Method in Solid Mechanics,* Allen and Unwin.

Feigl, K.L. *et al.*, 2002. Estimating slip distribution for the Izmit mainshock from coseismic GPS, ERS-1, RADARSAT, and SPOT measurements, *Bull. seism. Soc. Am.,* **92**(February), 138–160.

Gimbutas, Z., Greengard, L., Barall, M. & Tullis, T.E., 2012. On the calculation of displacement, stress, and strain induced by triangular dislocations, *Bull. seism. Soc. Am.,* **102**(6), 2776–2780.

Hirth, J.P. & Lothe, J., 1982. *Theory of Dislocations,* 2nd edn, John Wiley & Sons.

Jeyakumaran, M., Rudnicki, J.W. & Keer, L.M., 1992. Modeling slip zones with triangular dislocation elements, *Bull. seism. Soc. Am.,* **82**(5), 2153–2169.

Kelvin, S.W.T., 1848. Note on the integration of the equations of equilibrium of an elastic solid, *Cambridge Dublin Math. J.,* **3**(76-99), 87–89.

Kuriyama, K. & Mizuta, Y., 1993. Three-dimensional elastic analysis by the displacement discontinuity method with boundary division into triangular leaf elements, *Int. J. Rock Mech. Mining Sci. Geomech. Abstr.,* **30**(2), 111–123.

Love, A.E.H., 1944. *A Treatise on the Mathematical Theory of Elasticity,* Dover Publications.

Maerten, F., Resor, P., Pollard, D. & Maerten, L., 2005. Inverting for slip on three-dimensional fault surfaces using angular dislocations, *Bull. seism. Soc. Am.,* **95**(5), 1654–1665.

Meade, B.J., 2007. Algorithms for the calculation of exact displacements, strains, and stresses for triangular dislocation elements in a uniform elastic half space, *Comput. Geosci.,* **33**(8), 1064–1075.

Mindlin, R.D., 1936. Force at a point in the interior of a semi-infinite solid, *Physics,* **7**(5), 195–202.

Okada, Y., 1985. Surface deformation due to shear and tensile faults in a half-space, *Bull. seism. Soc. Am.,* **75**(4), 1135–1154.

Okada, Y., 1992. Internal deformation due to shear and tensile faults in a half-space, *Bull. seism. Soc. Am.,* **82**(2), 1018–1040.

Segall, P., 1997. New insights into old earthquakes, *Nature,* **388**(July), 122–123.

Segall, P., 2010. *Earthquake and Volcano Deformation,* Princeton Univ. Press.

Steketee, J.A., 1958. On Volterra's dislocations in a semi-infinite elastic medium, *Can. J. Phys.,* **36**(2), 192–205.

Thomas, A.L., 1993. POLY3D: a three-dimensional, polygonal element, displacement discontinuity boundary element computer program with applications to fractures, faults, and cavities in the Earth's, *Master's thesis,* Stanford University.

Ungar, A.A., 2010. *Barycentric Calculus in Euclidean and Hyperbolic Geometry: A Comparative Introduction,* World Scientific Publishing Co. Pte. Ltd.

Van Oosterom, A. & Strackee, J., 1983. The solid angle of a plane triangle, *IEEE Trans. Biomed. Eng.,* **30**(2), 125–126.

Volterra, V., 1907. Sur l'équilibre des corps élastiques multiplement connexes, *Annal. Sci. de l'Ecole Norm. Supér.,* **24,** 401–517.

Wald, D.J. & Heaton, T.H., 1994. Spatial and temporal distribution of slip for the 1992 Landers, California, earthquake, *Bull. seism. Soc. Am.,* **84**(3), 668–691.

Yoffe, E.H., 1960. The angular dislocation, *Philos. Mag.,* **5**(50), 161–175.

APPENDIX A: GENERAL SCHEME FOR THE COORDINATE TRANSFORMATION

To transform coordinates between two Cartesian coordinate systems, we utilize vector linear algebra operations. By using this method, we can avoid the presence of rotation matrices in the equations and perform the transformations more efficiently using a single transformation matrix rather than three rotation matrices. If $\{\vec{e}_1, \vec{e}_2, \vec{e}_3\}$ and $\{\vec{f}_1, \vec{f}_2, \vec{f}_3\}$ are two arbitrary orthonormal bases for $\mathbb{R}^3$ that represent two Cartesian coordinate systems, then any arbitrary vector $\vec{r}$ can be represented as a linear combination of the basis vectors as follows:

$$\vec{r} = \gamma_1\vec{e}_1 + \gamma_1\vec{e}_2 + \gamma_1\vec{e}_3 \tag{A1}$$

or

$$\vec{r} = \delta_1\vec{f}_1 + \delta_1\vec{f}_2 + \delta_1\vec{f}_3. \tag{A2}$$

We define $r_1 = (\gamma_1\,\gamma_2\,\gamma_3)^T$ and $r_2 = (\delta_1\,\delta_2\,\delta_3)^T$ as the coordinates of $\vec{r}$ in the first and second coordinate systems, respectively. If the columns of the matrix

$$A = \begin{pmatrix} m_1 & n_1 & k_1 \\ m_2 & n_2 & k_2 \\ m_3 & n_3 & k_3 \end{pmatrix}$$

represent the coordinates of $\vec{e}_1$, $\vec{e}_2$ and $\vec{e}_3$ in the second coordinate system, then we can write

$$\begin{cases} \vec{e}_1 = m_1\vec{f}_1 + m_2\vec{f}_2 + m_3\vec{f}_3 \\ \vec{e}_2 = n_1\vec{f}_1 + n_2\vec{f}_2 + n_3\vec{f}_3 \\ \vec{e}_3 = k_1\vec{f}_1 + k_2\vec{f}_2 + k_3\vec{f}_3 \end{cases}.$$

Substituting these terms into eq. (A1) and regrouping the result, we obtain

$$\vec{r} = (\gamma_1 m_1 + \gamma_2 n_1 + \gamma_3 k_1)\,\vec{f}_1 + (\gamma_1 m_2 + \gamma_2 n_2 + \gamma_3 k_2)\,\vec{f}_2 + (\gamma_1 m_3 + \gamma_2 n_3 + \gamma_3 k_3)\,\vec{f}_3,$$

which, using matrix notation, can be written as

$$r_2 = Ar_1. \tag{A3}$$

Therefore, eq. (A3) performs the direct vector transformation from the first coordinate system into the second, and the matrix A is the transformation matrix. Note that eq. (A3) is used only for the transformation of free vectors, such as displacement vectors, which do not depend on the origin of the coordinate system. For the transformation of a position vector of a calculation point or a TD vertex, we use the following equation:

$$r_2 = Ar_1 + r_{02}, \tag{A4}$$

where r_{02} is the translation matrix and includes the coordinates of the origin of the first coordinate system in the second coordinate system. Moreover, because of the orthonormality of the bases, it is straightforward to show that $AA^T = AA^{-1} = I$, where I is the identity matrix. Therefore, the inverse vector transformation for a displacement vector will be

$$r_1 = A^T r_2. \tag{A5}$$

Similarly, we write the inverse vector transformation for a position vector as

$$r_1 = A^T r_2 + r_{01}, \tag{A6}$$

where r_{01} is the translation matrix, which includes the coordinates of the origin of the second coordinate system in the first coordinate system. By substituting eq. (A6) into eq. (A4), it is straightforward to show that

$$r_{02} = -Ar_{01}, \tag{A7}$$

or equivalently,

$$r_{01} = -A^T r_{02}. \tag{A8}$$

When eq. (A8) is substituted into eq. (A6), the latter can be written in the form

$$r_1 = A^T(r_2 - r_{02}), \tag{A9}$$

which can be used independently from eq. (A6) whenever r_{02} is given.

Finally, the transformation equation for a second-rank tensor S_1 from the first coordinate system into the second is as follows (Segall 2010):

$$S_2 = AS_1A^T. \tag{A10}$$

APPENDIX B: THE ANGULAR DISLOCATION EQUATIONS

Yoffe (1960) developed the equations for the displacement and stress fields of an angular dislocation in a full-space, as illustrated in Fig. 1(a). Here, we provide the complete set of these equations, which we have corrected for a few misprints (in bold). In the following, (x, y, z) are the coordinates of the calculation point, (b_x, b_y, b_z) are the coordinates of the slip vector, and φ is the Burgers function at the calculation point corresponding to the angular dislocation (Yoffe 1960), which can be calculated using eq. (10) in Section 2.3.

For each component of the displacement vector (u, v, w), we consider the contributions of the slip vector components separately, as follows:

$$u_x = \frac{b_x}{8\pi(1-\nu)}\left[\frac{xy}{r(r-z)} - \frac{x\eta}{r(r-\zeta)}\right]$$

$$v_x = \frac{b_x}{8\pi(1-\nu)}\left[\frac{\eta\sin\alpha}{r-\zeta} - \frac{y\eta}{r(r-\zeta)} + \frac{y^2}{r(r-z)} + (1-2\nu)(\cos\alpha\ln(r-\zeta) - \ln(r-z))\right]$$

$$w_x = \frac{b_x}{8\pi(1-\nu)}\left[\frac{\eta\cos\alpha}{r-\zeta} - \frac{y}{r} - \frac{\eta z}{r(r-\zeta)} - (1-2\nu)\sin\alpha\ln(r-\zeta)\right]$$

$$u_y = \frac{b_y}{8\pi(1-\nu)}\left[\frac{x^2\cos\alpha}{r(r-\zeta)} - \frac{x^2}{r(r-z)} - (1-2\nu)(\cos\alpha\ln(r-\zeta) - \ln(r-z))\right]$$

$$v_y = \frac{b_y x}{8\pi(1-\nu)}\left[\frac{y\cos\alpha}{r(r-\zeta)} - \frac{\sin\alpha\cos\alpha}{r-\zeta} - \frac{y}{r(r-z)}\right]$$

$$w_y = \frac{b_y x}{8\pi(1-\nu)}\left[\frac{z\cos\alpha}{r(r-\zeta)} - \frac{\cos^2\alpha}{r-\zeta} + \frac{1}{r}\right]$$

$$u_z = \frac{b_z\sin\alpha}{8\pi(1-\nu)}\left[(1-2\nu)\ln(r-\zeta) - \frac{x^2}{r(r-\zeta)}\right]$$

$$v_z = \frac{b_z x\sin\alpha}{8\pi(1-\nu)}\left[\frac{\sin\alpha}{r-\zeta} - \frac{y}{r(r-\zeta)}\right]$$

$$w_z = \frac{b_z x\sin\alpha}{8\pi(1-\nu)}\left[\frac{\cos\alpha}{r-\zeta} - \frac{z}{r(r-\zeta)}\right], \tag{B1}$$

where $\eta = y\cos\alpha - z\sin\alpha$, $\zeta = y\sin\alpha + z\cos\alpha$, $r = \sqrt{x^2+y^2+z^2}$ and ν is the Poisson's ratio.

Now, if we define the 'incomplete' displacement vector components as

$$u^0 = u_x + u_y + u_z$$

$$v^0 = v_x + v_y + v_z$$

$$w^0 = w_x + w_y + w_z, \tag{B2}$$

then the complete displacement vector components can be calculated as follows:

$$u = b_x\varphi + u^0$$

$$v = b_y\varphi + v^0$$

$$w = b_z\varphi + w^0. \tag{B3}$$

By comparing eqs (B2) and (B3), it can be observed that the final displacements are the sum of the incomplete displacements and the product of the slip vector (b_x, b_y, b_z) with the Burgers function φ.

The strain-field equations are functions of the partial derivatives of the displacements. The final strain equations, after the simplification and regrouping of several algebraic terms in the partial derivatives of the displacements, can be represented as follows:

$$\epsilon_{xx} = b_x \frac{\partial \varphi}{\partial x} + \frac{b_x}{8\pi(1-\nu)}\left[\frac{\eta}{\xi r} + \frac{\eta x^2}{\xi^2 r^2} - \frac{\eta x^2}{\xi r^3} + \frac{y}{r(r-z)} - \frac{x^2 y}{r^2(r-z)^2} - \frac{x^2 y}{r^3(r-z)}\right]$$

$$- \frac{b_y x}{8\pi(1-\nu)}\left[\left(\frac{2\nu+1}{\xi r} + \frac{x^2}{\xi^2 r^2} - \frac{x^2}{\xi r^3}\right)\cos\alpha + \frac{2\nu+1}{r(r-z)} - \frac{x^2}{r^2(r-z)^2} - \frac{x^2}{r^3(r-z)}\right]$$

$$+ \frac{b_z x \sin\alpha}{8\pi(1-\nu)}\left(\frac{2\nu+1}{\xi r} + \frac{x^2}{\xi^2 r^2} - \frac{x^2}{\xi r^3}\right)$$

$$\epsilon_{yy} = b_y \frac{\partial \varphi}{\partial y} + \frac{b_x}{8\pi(1-\nu)}\left[\left(\frac{1}{\xi r} + \frac{(r\sin\alpha - y)^2}{\xi^2 r^2} - \frac{y^2}{\xi r^3}\right)\eta + \frac{(2\nu+1)\,y}{r(r-z)} - \frac{y^3}{r^2(r-z)^2} - \frac{y^3}{r^3(r-z)}\right.$$

$$\left. - \frac{2\nu\cos\alpha\,(r\sin\alpha - y)}{\xi r}\right] - \frac{b_y x}{8\pi(1-\nu)}\left[\frac{1}{r(r-z)} - \frac{y^2}{r^2(r-z)^2} - \frac{y^2}{r^3(r-z)}\right.$$

$$\left. + \left(\frac{1}{\xi r} + \frac{(r\sin\alpha - y)^2}{\xi^2 r^2} - \frac{y^2}{\xi r^3}\right)\cos\alpha\right] + \frac{b_z x \sin\alpha}{8\pi(1-\nu)}\left[\frac{1}{\xi r} + \frac{(r\sin\alpha - y)^2}{\xi^2 r^2} - \frac{y^2}{\xi r^3}\right]$$

$$\epsilon_{zz} = b_z \frac{\partial \varphi}{\partial z} + \frac{b_x}{8\pi(1-\nu)}\left[\frac{\eta}{\xi r} + \frac{\eta(r\cos\alpha - z)^2}{\xi^2 r^2} - \frac{\eta z^2}{\xi r^3} + \frac{yz}{r^3} + \frac{2\nu\sin\alpha\,(r\cos\alpha - z)}{\xi r}\right]$$

$$- \frac{b_y x}{8\pi(1-\nu)}\left[\left(\frac{1}{\xi r} + \frac{(r\cos\alpha - z)^2}{\xi^2 r^2} - \frac{z^2}{\xi r^3}\right)\cos\alpha + \frac{z}{r^3}\right]$$

$$+ \frac{b_z x \sin\alpha}{8\pi(1-\nu)}\left[\frac{1}{\xi r} + \frac{(r\cos\alpha - z)^2}{\xi^2 r^2} - \frac{z^2}{\xi r^3}\right]$$

$$\epsilon_{xy} = \frac{1}{2}b_x \frac{\partial \varphi}{\partial y} + \frac{1}{2}b_y \frac{\partial \varphi}{\partial x} - \frac{b_x}{8\pi(1-\nu)}\left[\frac{xy^2}{r^2(r-z)^2} - \frac{\nu x}{r(r-z)} + \frac{xy^2}{r^3(r-z)} - \frac{\nu x\cos\alpha}{\xi r} + \frac{\eta x(r\sin\alpha - y)}{\xi^2 r^2} + \frac{\eta x y}{\xi r^3}\right]$$

$$+ \frac{b_y}{8\pi(1-\nu)}\left[\frac{x^2 y}{r^2(r-z)^2} - \frac{\nu y}{r(r-z)} + \frac{x^2 y}{r^3(r-z)} + \frac{\nu\cos\alpha\,(r\sin\alpha - y)}{\xi r}\right.$$

$$\left. + \frac{x^2\cos\alpha\,(r\sin\alpha - y)}{\xi^2 r^2} + \frac{x^2 y\cos\alpha}{\xi r^3}\right] - \frac{b_z\sin\alpha}{8\pi(1-\nu)}\left[\frac{\nu(r\sin\alpha - y)}{\xi r} + \frac{x^2(r\sin\alpha - y)}{\xi^2 r^2} + \frac{x^2 y}{\xi r^3}\right]$$

$$\epsilon_{xz} = \frac{1}{2}b_x \frac{\partial \varphi}{\partial z} + \frac{1}{2}b_z \frac{\partial \varphi}{\partial x} - \frac{b_x}{8\pi(1-\nu)}\left[-\frac{xy}{r^3} + \frac{\boldsymbol{\nu} x\sin\alpha}{\xi r} + \frac{\eta x\cos\alpha}{\xi^{\mathbf{2}} r} - \frac{\eta x z}{\xi^2 r^2} + \frac{\eta x z}{\xi r^3}\right]$$

$$+ \frac{b_y}{8\pi(1-\nu)}\left[-\frac{x^2}{r^3} + \frac{\nu}{r} + \frac{\nu\cos\alpha\,(r\cos\alpha - z)}{\xi r} + \frac{x^2\cos\alpha\,(r\cos\alpha - z)}{\xi^2 r^2} + \frac{x^2 z\cos\alpha}{\xi r^3}\right]$$

$$- \frac{b_z\sin\alpha}{8\pi(1-\nu)}\left[\frac{\nu(r\cos\alpha - z)}{\xi r} + \frac{x^2(r\cos\alpha - z)}{\xi^2 r^2} + \frac{x^2 z}{\xi r^3}\right]$$

$$\epsilon_{yz} = \frac{1}{2}b_y\frac{\partial\varphi}{\partial z} + \frac{1}{2}b_z\frac{\partial\varphi}{\partial y} + \frac{b_x}{8\pi\,(1-\nu)}\left[\frac{y^2}{r^3} - \frac{\nu}{r} - \frac{\nu\cos\alpha\,(r\cos\alpha - z)}{\xi r} + \frac{\nu\sin\alpha\,(r\sin\alpha - y)}{\xi r} + \frac{\eta\sin\alpha\cos\alpha}{\xi^2}\right.$$
$$\left. - \frac{\eta\,(y\cos\alpha + z\sin\alpha)}{\xi^2 r} + \frac{\eta y z}{\xi^2 r^2} - \frac{\eta y z}{\xi r^3}\right] - \frac{b_y x}{8\pi\,(1-\nu)}\left[\frac{y}{r^3} + \frac{\sin\alpha\cos^2\alpha}{\xi^2} - \frac{\cos\alpha\,(y\cos\alpha + z\sin\alpha)}{\xi^2 r}\right.$$
$$\left. + \frac{yz\cos\alpha}{\xi^2 r^2} - \frac{yz\cos\alpha}{\xi r^3}\right] - \frac{b_z x\sin\alpha}{8\pi\,(1-\nu)}\left[\frac{yz}{\xi r^3} - \frac{\sin\alpha\cos\alpha}{\xi^2} + \frac{y\cos\alpha + z\sin\alpha}{\xi^2 r} - \frac{yz}{\xi^2 r^2}\right], \tag{B4}$$

where $\xi = y\sin\alpha + z\cos\alpha - r$.

The partial derivatives of the Burgers function, that is $\frac{\partial\varphi}{\partial x}$, $\frac{\partial\varphi}{\partial y}$ and $\frac{\partial\varphi}{\partial z}$, which appear in eq. (B4), must be calculated from eq. (11) in Section 2.3.

Finally, the stresses can be calculated using the isotropic form of Hooke's law (Segall 2010):

$$\sigma_{xx} = 2\mu\epsilon_{xx} + \lambda\left(\epsilon_{xx} + \epsilon_{yy} + \epsilon_{zz}\right)$$
$$\sigma_{yy} = 2\mu\epsilon_{yy} + \lambda\left(\epsilon_{xx} + \epsilon_{yy} + \epsilon_{zz}\right)$$
$$\sigma_{zz} = 2\mu\epsilon_{zz} + \lambda\left(\epsilon_{xx} + \epsilon_{yy} + \epsilon_{zz}\right)$$
$$\sigma_{xy} = 2\mu\epsilon_{xy}$$
$$\sigma_{xz} = 2\mu\epsilon_{xz}$$
$$\sigma_{yz} = 2\mu\epsilon_{yz}, \tag{B5}$$

where μ and λ are the Lamé coefficients; μ is the shear modulus.

APPENDIX C: THE BARYCENTRIC COORDINATE SYSTEM

The barycentric coordinate system is an efficient way to represent the coordinates of points in the plane of a triangle with respect to its vertices. The very simple and often symmetric form of the equations of geometric objects in this coordinate system makes it the most appropriate system for many problems in analytical geometry and computer sciences that are related to the geometrical properties of a triangle (Bottema 2008).

It is well known from mechanics that for a point G that is the centre of mass, or the barycentre, of three masses m_1, m_2 and m_3 that are attached to the vertices of a triangle $A_1A_2A_3$, respectively, we can write

$$\vec{r}_G = \frac{m_1\vec{r}_1 + m_2\vec{r}_2 + m_3\vec{r}_3}{m_1 + m_2 + m_3}, \tag{C1}$$

where all vectors are the position vectors in an arbitrary 2-D coordinate system in the plane of the triangle. By generalizing this concept to include negative weights as well, the barycentric coordinates of an arbitrary point P in the plane of an arbitrary triangle $A_1A_2A_3$ with respect to this triangle can be regarded as the ordered triple (m_1, m_2, m_3), which is composed of the weights that are placed on the vertices of $A_1A_2A_3$; point P then becomes the centre of mass of the system of masses (Ungar 2010). Here, we use the normalized barycentric coordinates (μ_1, μ_2, μ_3), also known as areal coordinates, which are calculated by dividing each coordinate by the sum of all three (Coxeter 1969); we can then write

$$\mu_1 + \mu_2 + \mu_3 = 1, \tag{C2}$$

where

$$\mu_i = \frac{m_i}{\sum_{i=1}^{3} m_i}, \tag{C3}$$

for $i = 1, 2, 3$.

Considering eq. (C1) for point P together with eq. (C2), we obtain

$$\begin{pmatrix} x_P \\ y_P \end{pmatrix} = \begin{pmatrix} \mu_1 x_1 + \mu_2 x_2 + (1-\mu_1-\mu_2)\,x_3 \\ \mu_1 y_1 + \mu_2 y_2 + (1-\mu_1-\mu_2)\,y_3 \end{pmatrix}, \tag{C4}$$

or equivalently,

$$\begin{pmatrix} \mu_1 \\ \mu_2 \end{pmatrix} = \begin{pmatrix} x_1 - x_3 & x_2 - x_3 \\ y_1 - y_3 & y_2 - y_3 \end{pmatrix}^{-1} \begin{pmatrix} x_P \\ y_P \end{pmatrix}. \tag{C5}$$

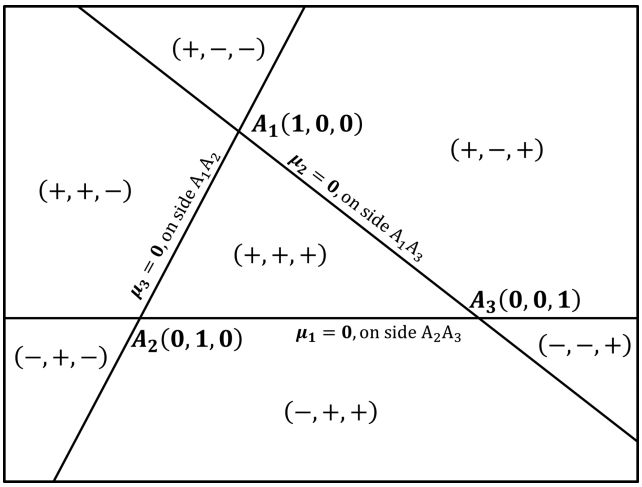

Figure C1. Geometrical properties of the barycentric coordinate system. The barycentric coordinates of the vertices, the equations of the sides and the signs of the components of the barycentric coordinates of the points in the various partitions delimited by the sides of the triangle $A_1A_2A_3$.

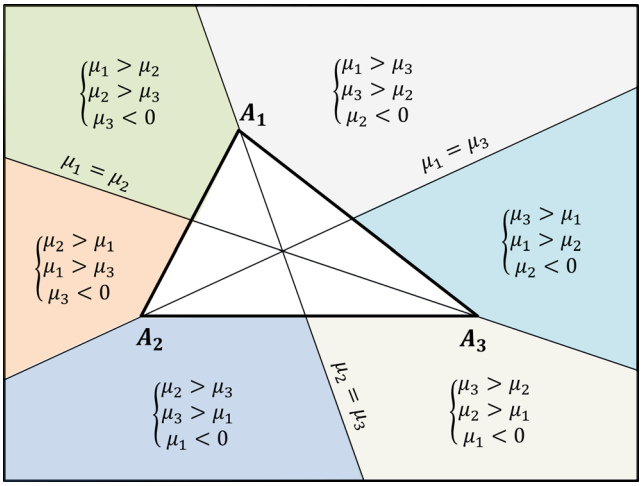

Figure C2. Certain geometrical properties of the barycentric coordinate system. The equations of the medians of the triangle $A_1A_2A_3$ and the inequalities that define the partitions illustrated in Fig. 4.

It is now quite straightforward to calculate μ_3 from eq. (C2) after replacing μ_1 and μ_2 with their values calculated from eq. (C5). Note that although the barycentric coordinates are expressed in terms of three components, they represent the position of a point in a 2-D space. This fact is also indicated by eq. (C2), which shows that these components are not independent.

We summarize certain properties of the normalized barycentric coordinate system in Figs C1 and C2. Independent of the Cartesian coordinates of the vertices, the normalized barycentric coordinates of the vertices are always (1, 0, 0), (0, 1, 0) and (0, 0, 1), and $\mu_i = 0$ is the equation of the line that contains the side opposite to vertex A_i, for $i = 1, 2, 3$ (Ungar 2010). The plus and minus signs in the parentheses in Fig. C1 represent the signs of the barycentric coordinates of the points in each of the partitions formed by these lines, which pass through each pair of vertices in the plane of the triangle $A_1A_2A_3$. Each of the other partitions in Fig. C2, which are formed by the medians of the triangle $A_1A_2A_3$, is represented by a set of three simple inequalities. It is also trivial to show that $\mu_1 = \mu_2$, $\mu_1 = \mu_3$ and $\mu_2 = \mu_3$ are the equations of the medians (Ungar 2010).

SUPPORTING INFORMATION

Additional Supporting Information may be found in the online version of this paper:

(http://gji.oxfordjournals.org/lookup/suppl/doi:10.1093/gji/ggv035/-/DC1).

Please note: Oxford University Press is not responsible for the content or functionality of any supporting materials supplied by the authors. Any queries (other than missing material) should be directed to the corresponding author for the paper.